

University of Texas Rio Grande Valley

ScholarWorks @ UTRGV

Theses and Dissertations - UTRGV

8-2023

Two-Dimensional Nanomaterials and Nanocomposites for Sensing, Separation, and Energy Applications

Md Ashiqur Rahman

The University of Texas Rio Grande Valley

Follow this and additional works at: <https://scholarworks.utrgv.edu/etd>



Part of the [Mechanical Engineering Commons](#), and the [Nanoscience and Nanotechnology Commons](#)

Recommended Citation

Rahman, Md Ashiqur, "Two-Dimensional Nanomaterials and Nanocomposites for Sensing, Separation, and Energy Applications" (2023). *Theses and Dissertations - UTRGV*. 1391.

<https://scholarworks.utrgv.edu/etd/1391>

This Thesis is brought to you for free and open access by ScholarWorks @ UTRGV. It has been accepted for inclusion in Theses and Dissertations - UTRGV by an authorized administrator of ScholarWorks @ UTRGV. For more information, please contact justin.white@utrgv.edu, william.flores01@utrgv.edu.

TWO-DIMENSIONAL NANOMATERIALS AND NANOCOMPOSITES FOR SENSING,
SEPARATION, AND ENERGY APPLICATIONS

A Thesis

by

MD ASHIQUR RAHMAN

Submission in Partial Fulfillment of the
Requirements for the degree of
MASTER OF SCIENCE IN ENGINEERING

Major Subject: Mechanical Engineering

The University of Texas Rio Grande Valley

August 2023

TWO-DIMENSIONAL NANOMATERIALS AND NANOCOMPOSITES FOR SENSING,
SEPARATION, AND ENERGY APPLICATIONS

A Thesis
by
MD ASHIQUR RAHMAN

COMMITTEE MEMBERS

Dr. Ali Ashraf
Chair of Committee

Dr. Karen Lozano
Committee Member

Dr. Mataz Alcoutlabi
Committee Member

August 2023

Copyright 2023 Md Ashiqur Rahman

All Rights Reserved

ABSTRACT

Rahman, Md Ashiqur, Two-dimensional Nanomaterials and Nanocomposites for Sensing, Separation, and Energy Applications. Master of Science in Engineering (MSE), August, 2023, 76 pp., 6 tables, 28 figures, references, 150 titles.

Two-dimensional (2D) nanomaterials have gained popularity over the last few decades due to their excellent mechanical, electrical, and thermal properties. These unique properties of 2D nanomaterials can be exploited in various applications specially in sensor, energy, and separation devices. In this study, the sensing and energy generation performance of PVDF/PAni fiber mat systems is made by the forcespinning method with and without graphene coating. The graphene-coated nanocomposites show an average output voltage of 75 mV (peak-to-peak) which is 300% higher compared to bare fiber mats and an output current of 24 mA (peak-to-peak) by gentle finger pressing. Moreover, the graphene-coated PVDF/PAni was investigated as a promising system for temperature, vibration, and airflow sensing, as well as a water tide energy harvesting piezoelectric nanogenerator. Additionally, a low-cost, single-step, sophisticated graphene-enhanced elastomeric nanocomposite was fabricated for multifunctional sensing and device fabrication by using a shear batch mixer. A direct ink writing of the prepared ink was used for fabricating a membrane on a metal mesh substrate. Furthermore, the study also showed the enhanced battery performance of chemical vapor-deposited pyrolytic carbon coatings on nanoparticles and nanofibers.

DEDICATION

All praises go to Almighty Allah, whose blessings enabled me to complete both this work and my graduate studies. I would like to dedicate this thesis to my parents, Md Munsur Ali and Afiya Begum, who are my inspirations and whose unconditional love and support have helped me achieve my life goals. I'd also like to thank my wonderful wife, Naznin Sultana, for her love, compassion, and sacrifice, as well as my younger sister Suraiya Yeasmin and her child Md Rafin Rezwan, whom I adore most.

ACKNOWLEDGMENTS

I am grateful to my advisor, Dr. Ali Ashraf, who is not only a great mentor but also a great human being. My motivation to work on research projects came from his unconditional support beginning on the day I arrived in the United States. I will be forever thankful to my advisor for all his guidance and help, and his unwavering support paved the way for me to achieve my goals.

Words cannot explain how grateful I am to my thesis committee members, Dr. Karen Lozano, and Dr. Mataz Alcoutlabi, for their invaluable support throughout the degree. It was a delight to be able to work on such exciting projects at Dr. Lozano's Nanotechnology Center and in Dr. Alcoutlabi's lab. I would like to thank Dr. Farid Ahmed, and Dr. Victoria Padilla for helping me to analyze different characterization and experimental results.

I would like to express my gratitude to Dr. Nazmul Islam for his support throughout my graduate study at UTRGV. Additionally, this endeavor would not have been possible without the generous support from the College of Engineering & Computer Science (for awarding me the prestigious Presidential Research Fellowship) and National Science Foundation (NSF), who financed the research work. I am also thankful to my lab mates Dipannita Ghosh, Md. Abdur Rahman Bin Abdus Salam, Elmmmer Vera Alvarado, Javier Becerril for their fruitful advice and help during the projects. I am also grateful to Md Shahriar Forhad, Dipasree Bhowmick, and David Sanchez for helping in analyzing different characterizations. Last of all, I am indebted to all the individuals who helped me during this journey.

TABLE OF CONTENTS

	Page
ABSTRACT.....	iii
DEDICATION.....	iv
ACKNOWLEDGMENTS	v
TABLE OF CONTENTS.....	vi
LIST OF TABLES.....	viii
LIST OF FIGURES	ix
CHAPTER I. INTRODUCTION.....	1
Background Study of Graphene Coated Fiber Mat.....	3
Background Study of Graphene Conductive Polymer Paper Biosensor	6
Background Study of Shear Exfoliated 2D Nanocomposites	10
CHAPTER II. 2D NANOMATERIAL AND NANOCOMPOSITE BASED SENSING	
DEVICES.....	14
Strain or Electromechanical Sensing	14
Nanofiber-Based Sensing	14
In-Situ Shear Exfoliated Graphene Nanocomposites for Sensing.....	25
Paper Based Electrochemical Sensing for Biomolecules Detection	31
Sensor and Ink Preparation.....	31
Biomolecules Detection Using Paper Based Sensor	36

CHAPTER III. 2D NANOMATERIAL BASED ENERGY GENERATION/STORAGE	
DEVICES.....	44
Nanogeneration Using Nanofiber Composite	44
Nanogeneration Using Water Waves	44
Vibration Analysis.....	46
CVD Coated Nanofiber Anode for Enhanced Battery Performance	50
CVD Carbon Coatings.....	50
Characterization.....	51
CHAPTER IV. NANOCOMPOSITE INK BASED SEPARATION DEVICES	55
Direct Ink Writing of Polymer Nanocomposite Membrane.....	55
Fabrication of Ink	55
Printing Parameters Optimization	56
Testing of 3D Printed Membrane.....	58
Fabrication and Characterization.....	58
Performance of DIW printed Metal Mesh Membrane	61
DIW Printed Membrane with Laser Treatment and Electrical Current	62
CHAPTER V. CONCLUSION.....	64
REFERENCES	66
BIOGRAPHICAL SKETCH	76

LIST OF TABLES

	Page
Table 1: Comparison of dopamine detection performance for different electrochemical biosensors based on conductive polymers.	40
Table 2: Comparison of TNF- α detection of some electrochemical biosensors using different techniques.....	41
Table 3: Peristaltic Pump characteristic flow rate with control time.....	44
Table 4: Performance of different nanocomposite nanogenerators based on PVDF.....	45
Table 5: Performance differences between PVDF/PAni and G@PVDF/PANI for all sensing and nanogeneration applications.....	49
Table 6: Optimized parameters for printing on a 20x20 Stainless Steel Metal Mesh as a Membrane for water desalination.	57

LIST OF FIGURES

	Page
Figure 1: (a) Nanomaterials synthesis: top-down and bottom-up approaches.....	2
Figure 2: SEM images of PVDF/PAni fiber mat at a magnification	18
Figure 3: (a) X-Ray Diffraction (XRD) of G@PVDF/PAni and PVDF/PAni	19
Figure 4: Current-Voltage (I-V) characteristics of the conductive PVDF/PAni	20
Figure 5: (a) Temperature sensing setup having Fluke RSE 600 thermal camera.....	22
Figure 6: (a) Open-circuit voltage (V_{OC}) of PVDF/PAni nanofiber	23
Figure 7: (a) Open-circuit voltage (V_{OC}) of G@PVDF/PAni.....	24
Figure 8: (a) Schematic of shear exfoliation of graphite and G-EMC fabrication	28
Figure 9: (a) I-V characteristics plot for 40 wt. % G-EMC sensor.....	29
Figure 10: (a) Pulse, (b) Breathing, and (c) Speech detection using G-EMC sensor.	30
Figure 11: Schematic of (a) G-PEDOT:PSS conductive polymer ink preparation	32
Figure 12: (a-d) Scanning electron microscopy images of GR-CP-paper-based sensor.	33
Figure 13: Single layer dip-coated paper-based biosensor (a) EIS characterization	36
Figure 14: Double layer dip-coated paper-based biosensor (a) EIS characterization.....	39
Figure 15: Paper-based biosensor (a) EIS characterization of TNF- α detection	42
Figure 16: Paper-based biosensors' (a) EIS characterization of IL-6 detection	43
Figure 17: Voltage signal for pump switch on 1000 ms and switch off 100 ms	47
Figure 18: (a) Setup image of sample and vibration motor, (b) Vibration (dB).....	48
Figure 19: Schematic of Chemical Vapor Deposition Setup	51

Figure 20: Recipe for pyrolytic carbon coating on SnO ₂ / TiO ₂ short fibers.	52
Figure 21: (a) Raman spectroscopy of pyrolytic carbon coated short nanofibers	53
Figure 22: Performance Analysis of CVD-coated SnO ₂ / TiO ₂ short fibers	54
Figure 23: (a) Schematic of high viscous Direct ink writing printing on metal mesh.....	57
Figure 24: Schematic of membrane distillation process	58
Figure 25: (a) Water contact angle at different locations of the membrane	59
Figure 26: CAD drawing of the membrane holder (a) top part, (b) bottom part	60
Figure 27: Performance of the metal mesh membrane. (a) flux and (b) rejection rate.....	61
Figure 28: Performance of the laser treated and electrical current applied metal mesh	63

CHAPTER I

INTRODUCTION

Two-dimensional (2D) nanomaterials are sophisticated materials that are atomically thick that consist of from single layer to a few layers. These materials have become attractive in different applications due to their unique mechanical, electrical, optical, and thermal properties. The properties may vary for the same nanomaterials, and it depends on the growth and synthesis process used for fabrication of the nanomaterials. For synthesizing 2D nanomaterials, two methods are used, top-down and bottom-up approaches (Figure 1. a). The top-down approach which involves breaking down of larger particles or flakes into atomistic scales. On the other hand, bottom-up approach accumulates particles or single atom to fabricate a larger structure.

In this study, different types of 2D nanomaterials synthesis and nanocomposite fabrication were introduced. The first study is about graphene (2D nanomaterial, hexagonal honeycomb lattice shown in Figure 1. b) which are a few atomic layers of graphite dip coated in polymer, polyvinylidene fluoride (PVDF). On the other hand, using shear exfoliation to break down the layered commercial graphite directly within the polymer precursor (elastomer - thermoset polymer) and curing agent is an example of top-down approach. Chemical vapor deposition of pyrolytic carbon on short fibers is a bottom-up approach as it produces single layer of graphene sheet and accumulates layer by layer (although pyrolytic carbon is turbostratic in nature as it has some rotation with basal plane). Commercial graphene with cellulose fibers and PEDOT:PSS polymer was used for biosensor fabrication. Finally, layered graphite material was

broken into smaller particles directly within elastomer using high shear planetary mixer, and this ink was then used for fabricating membrane on metal mesh using direct ink writing.

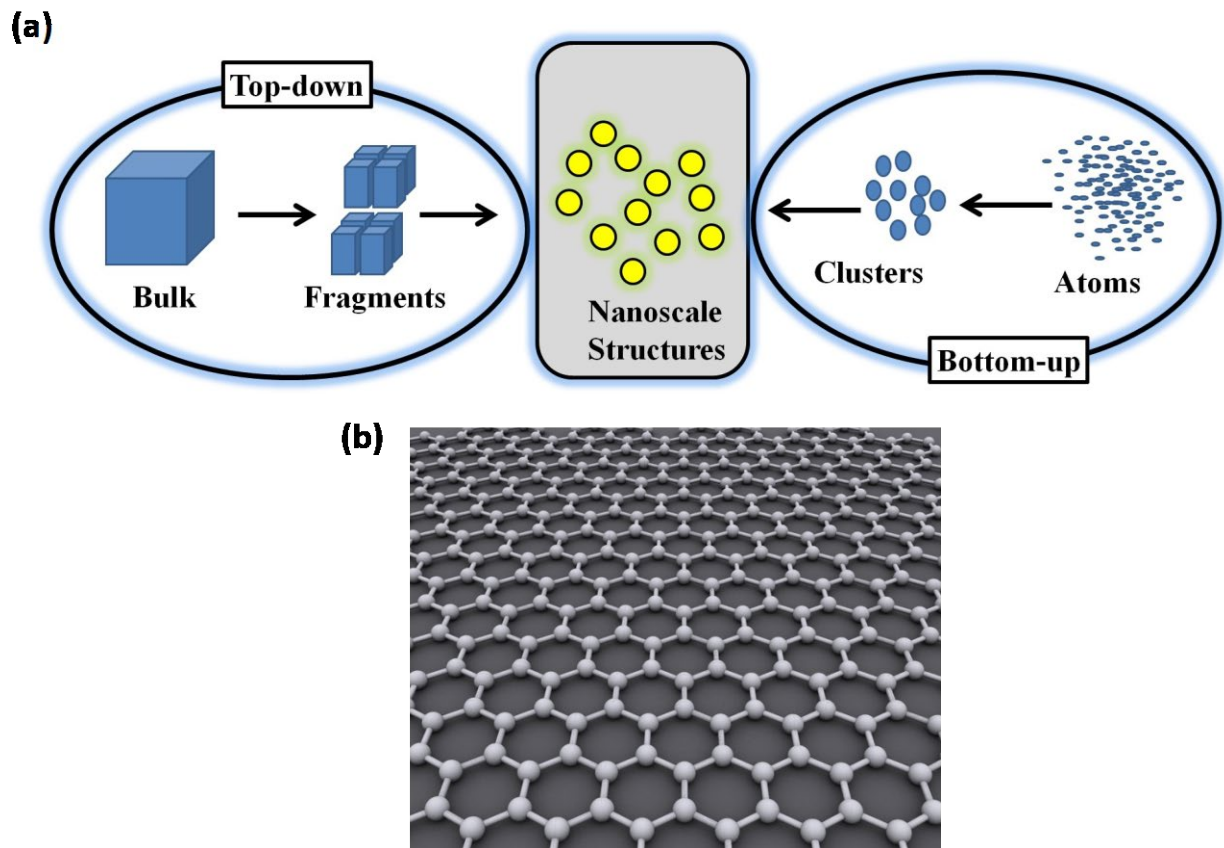


Figure 1: (a) Nanomaterials synthesis: top-down and bottom-up approaches, (b) Graphene hexagonal honeycomb lattice.

Background Study of Graphene Coated Fiber Mat

Polymers such as polyvinylidene fluoride (PVDF) and its copolymers have been widely used due to their piezoelectric properties (Broadhurst & Davis, 1984; Murayama et al., 1976; Ueberschlag, 2001; Vinogradov & Holloway, 1999; Zeng et al., 2013). PVDF is also described as a light, compliant material with high dielectric strength and attractive mechanical properties. PVDF fiber systems have been developed for a variety of applications such as pressure sensing (Lee & Sung, 1999; Shirinov & Schomburg, 2008; Y. Wang et al., 2011), temperature sensing (Pullano et al., 2017; Xia et al., 2018), vibration sensing (Pan et al., 2016), energy harvesting like nanogeneration (Briscoe & Dunn, 2015; Fan et al., 2016; Lu et al., 2020; Mahapatra et al., 2021), and biomedical applications (Guo et al., 2012; Moran et al., 2004; Mullaveetil et al., 2021). Many attempts have been made in the last few decades to develop nanoscale electrical power generators, with a variety of organic and inorganic materials being used as potential energy harvesters. Personal portable electronic devices, wireless sensing, and implantable biological devices can all be powered by these nanoscale electrical generators. Inorganic materials are brittle and have low formability, which limits their application. Polymeric electrical generators, on the other hand, have excellent formability and are lighter in weight, making them ideal for applications requiring flexibility. Asadnia *et al.* reported on single PVDF-based nanofiber sensor fabricated for piezoelectric and nanomechanical characterization as well as to detect oscillatory flow (Sengupta et al., 2017). Reports have also shown that the added presence of a conducting polymer to the PVDF system increases tensile strength and Young's modulus while decreasing elongation at break (Malmonge et al., 2010). Short conductive strands made of coated Multi-Wall Carbon Nano Tubes (MWCNTs) also aid in the formation of a conductive network in the nanofibers' transverse direction (Malmonge et al.,

2010). Merlini *et al.* demonstrated that PANi-coated electrospun PVDF mats portray interesting properties, including a three-dimensional fiber network structure and electrical conductivity(Merlini et al., 2015). The piezoelectric performance of a nanogenerator under various external mechanical stresses, such as pressure, tapping, and impact, was demonstrated by an electrospun PANi (polyaniline)/HNT (halloysite nanotube)/PVDF blend nanocomposite (Khalifa et al., 2019), though a low current as much as few μA was obtained. A highly flexible electrospun PVDF/PANi/g- C_3N_4 blend nanocomposite (PPBF) nanogenerator (size of $\sim 5.5 \text{ cm}^2$) for piezoelectric energy harvesting with maximum voltage and current output of 30 V and 3.7 μA , respectively, was successfully developed by Khalifa *et al.*(Khalifa & Anandhan, 2019). Yang *et al.* showed that graphene oxide integration (up to 2%) in PVDF increased the β phases of PVDF, and the short-circuit current and open-circuit voltage, values were 200nA and 1.5 V respectively(Yang et al., 2021).

ZnO nanoparticle-PVDF composite thin film demonstrated both enhanced energy generation and motion-sensing capabilities(Jin et al., 2020). Composites like SWCNT/a-PVDF are better in capacitive systems below a percolation threshold(Puértolas et al., 2017). None of them, however, reported a small PVDF-based fibers sample producing current output in the mA range which could be revolutionary for blue energy and vibration harvesting nanogenerators.

Forcespinning® is a centrifugal-action-based technology for producing nanofibers(Sarkar et al., 2010), the rotational speed of the spinneret, the design of the collection system, and the shape and size of the needles or nozzles are the controlled variables. Drop-casting is a simple technique where materials are mixed in a suitable solvent and cast by dropping on the target fiber/substrate. For example, Cha et al. used drop-casting to obtain CuO painted conductive woven textiles for improved energy storage(Cha et al., 2017). Vacuum filtration is a procedure

in which coating can be done via applying a pressure differential across the fiber/filter. Omi et al. developed a few layers of multiwalled carbon nanotubes (MWNTs) via vacuum filtration for a highly conductive ultrafiltration membrane to get high-quality water free from microorganisms(Omi et al., 2017). Dip-coating is a process by which material is submerged in coating and dried to make a coating. Highly conductive graphene-coated glass fibers were obtained from the dip-coating method by Fang et al(Fang et al., 2019). We used drop-casting for our experiment as this method is simple, and this is an efficient way for solvent-containing graphene (acetone) to be in contact with the fiber during a suitable period of time for mild etching, leading to the stronger attachment of graphene with fiber. In this work, PVDF/PAni fiber mats were developed utilizing the forcespinning method and subsequently coated with a graphene layer by two different solution drop-casting processes. The effect of graphene on the piezoelectric behavior of the nanocomposites was studied. The result indicated that the enhancement of electrical conductivity was achieved by the graphene nucleation sites within the conductive PVDF/PAni fiber mats. Acetone-based graphene drop-casting showed improved piezoelectric performance and hence using this nanofiber composite, the energy harvesting phenomena like nanogeneration using artificial tidal waves were studied. The electrical properties of spun PVDF/PAni fiber mats and their sensing performance as conductive mats depending on temperature, vibration, and flow were evaluated. The morphology and characterization of graphene-PVDF/PAni composites were also investigated.

Background Study of Graphene Conductive Polymer Paper Biosensor

Dopamine (DA) is one of the most important neurotransmitters in the human central nervous system. Dopamine deficiency may cause Parkinson's disease (Lotharius & Brundin, 2002), restless legs syndrome (Clemens et al., 2006), schizophrenia (Davis et al., 1991), and attention deficit hyperactivity disorder (ADHD) (J. Wu et al., 2012). Thus, sensitive, and selective dopamine detection using a simple and cost-effective method is highly desirable. On the other hand, cytokines, a class of regulatory proteins, are essential physiological and pathological markers for diagnosis of diseases (e.g., cancer and Alzheimer's) and response to injury. TNF- α , a pro-inflammatory cytokine originating from macrophages and monocytes, serves as an early sign of inflammatory disease and chronic wounds. The dysregulation of this cytokine can cause various types of diseases including rheumatoid arthritis (Caporali et al., 2009; Feldmann & Maini, 2001), cardiovascular disease (Popa et al., 2007), Alzheimer's disease (Maccioni et al., 2009), cancer (Balkwill, 2006; Cruceriu et al., 2020), and psoriasis (Cohen et al., 2007). TNF- α is considered an anti-cancer agent and its receptors can send both survival and death signals to cells. It ranges from 10 pg/mL in healthy human serum to ~2000 pg/mL in patients with chronic wounds (Baker & Leaper, 2000; Barrientos et al., 2008; Grayson et al., 1993; Grimstad et al., 2011; Russell et al., 2020). As a result, it is crucial to measure TNF- α in a quick, accurate, and simple manner to predict, assess, prevent, and monitor inflammation. Similarly, IL-6 is a multifunctional cytokine that plays an important role in immunomodulation, hematopoiesis, and inflammation. Dysregulated continual synthesis of IL-6 plays a pathological effect on chronic inflammation and autoimmunity including diabetes, rheumatoid arthritis, and cancer (Akbari & Hassan-Zadeh, 2018; Barton, 2001; Jengelly & Zimmers, 2022; Knüpfer &

Preiß, 2007; Pascual et al., 2000). Since the concentration of cytokines can be very small, a sensitive sensor is needed to detect them.

Electrochemical biosensors have certain advantages, such as ease of use, rapid, sensitive, and selective response even in complex environments (Anik, 2017; Munteanu & Apetrei, 2022). Additionally, electrochemical biosensors are inexpensive and can be miniaturized, and require small amounts of samples (Adabi et al., 2021). So, in the last few decades, the use of electrochemical biosensors has attracted the attention of the scientific community. To achieve a very low detection limit and selective detection of small biomarkers, modified electrodes have been employed. These electrodes include not only conductive polymers (Fabregat et al., 2014; Lakshmi et al., 2009; Weaver et al., 2014), but also carbon and metal nanomaterials (Alothman et al., 2010; Arumugasamy et al., 2020; Atta et al., 2019; Bala et al., 2019; Du et al., 2022; Xue et al., 2013; Yang et al., 2019), nanocomposites (Anuar et al., 2020; Choudhary et al., 2017; Pandikumar et al., 2014), ionic liquids (Rather et al., 2017; Zhu et al., 2010), and other materials. Conductive polymer electrodes such as poly(3,4-ethylenedioxythiophene) (PEDOT) (Mantione et al., 2017), polyaniline (PANI) (Morais et al., 2018), and polypyrrole (PPy) (Cho et al., 2020) have been widely used in electrochemical sensing due to their remarkable electrical conductivity, high signal transduction, mechanical flexibility, and chemical stability. Compared to PANI and Ppy, PEDOT shows relatively better stability, excellent charge transport, and higher conductivity. As PEDOT is insoluble in water or in common solvents (Rahimzadeh et al., 2020), PEDOT is synthesized in presence of poly(4-styrenesulfonate) (PSS). These two polymers generally referred to as PEDOT:PSS exhibits excellent solution-fabrication capability for dip coating. For conductive polymers, an optimized conductivity is needed for a lower signal-to-noise ratio (Hakimi et al., 2016). Graphene, which is an exceptional 2D nanomaterial due to its

excellent electrical, mechanical, and thermal properties, can be used as a filler for enhancing PEDOT:PSS conductivity, mechanical property, and high surface area for analyte conjugation (Karuwan et al., 2012).

PEDOT-Graphene modified electrodes provided a lower dopamine detection limit of 0.33 μM due to low oxidation potential (Xu et al., 2018). However, nanocomposites of PEDOT-Graphene Oxide (GO) showed no interference with uric acid and ascorbic acid for dopamine detection, and the detection limit was 39 nM (W. Wang et al., 2014). Field-effect transistors (FET) with modified PEDOT:PSS have also been used for dopamine detection (LOD - 6 μM), however, require complicated processing steps (Gualandi et al., 2016). On the other hand, the gold standard for cytokine detection is the enzyme-linked immunosorbent assay (ELISA), which depends on labeling and an optical read-out (Xie et al., 2021). So, impedance sensors can provide a promising avenue for miniature, rapid, and label-free detection of cytokine. For the last few decades, electrochemical sensors were developed to analyze quantitatively label-free TNF- α using different modified electrodes (Mazloun-Ardakani & Hosseinzadeh, 2015; Pui et al., 2013; Weng et al., 2013). However, due to excellent physical (mechanical flexibility, high strength) and chemical features (high solubility in water, conjugated π electrons with alternating single and multiple bonds) polymers are used widely to detect cytokines (Luong et al., 2020).

Paper, which is composed of numerous cellulose layers, is a popular substrate due to its low cost, lightweight, high abundance, environmental friendliness, and ease of bulk manufacture (Liang et al., 2019). So, paper has drawn much interest in sensor and device fabrication as it is flexible, portable, disposable, and easy to operate (Adkins et al., 2015; Cate et al., 2015; Dungchai et al., 2009, 2011; Liang et al., 2020; Mazzeo et al., 2021; Zou et al., 2018). Proper fabrication of electrochemical paper-based biosensors depends on the selection of paper material,

design of 2D and 3D electrodes, formation of a hydrophobic wall, surface modification of electrodes, and analyte conjugation (Loo & Pui, 2020). Whatman filter papers nos. 1 and 4, which are distinguished by porosity and particle retention, are used in a wide range of applications. Aidin *et al.* developed a sensitive biosensor using semi-conductive poly-(3-thiophene acetic acid) (P3) to determine TNF- α from human saliva and serum (Aydin et al., 2017). Wang *et al.* developed paper-based aptasensors fabricated with conductive polymer nanocomposite electrodes to detect cancer biomarkers (Wang et al., 2019). Furthermore, to get antigen-antibody conjugation, a graphene screen-printed electrode modified with polyaniline was used, and thus exhibited greater surface area for immobilization, and exceptional conductivity for human interferon-gamma (IFN- γ) detection (Ruecha et al., 2019). The sensor showed a better response over 5-1000 pg mL⁻¹ with a detection limit of 3.4 pg mL⁻¹. A paper-based biosensor with a carcinoembryonic antigen (CEA) detection range of 6-30 ng mL⁻¹, and a detection limit of 2.68 ng mL⁻¹ using PEDOT:PSS with modified filter paper was developed by Kumar *et al.* (Kumar et al., 2016). However, to the best of our knowledge, no paper-based biosensors have been reported for the detection of TNF- α , especially in a lower range by the scientific community. On the other hand, IL-6 detection can be done via direct (Russell et al., 2019), indirect competitive (Lou et al., 2014), and sandwiched nanoparticles labeled (Peng et al., 2011; G. Wang et al., 2011) electrochemical immunoassay methods.

In this paper, we fabricated a miniaturized graphene-PEDOT:PSS coated paper-based biosensor with laser engraving to detect dopamine, TNF- α , and IL-6. The method here used for coating is dip coating which is much more effective in terms of uniformity than the drop-casting method used in our previous work (Ghosh et al., 2022; Rahman, Rubaiya, et al., 2022). The electrodes were prepared by planetary mixed conductive G-PEDOT:PSS ink and Ag ink through

dip coating, and the performance was analyzed via electrochemical impedance spectroscopy. Towards that goal, we improved the viscosity and stability of the conductive ink by adjusting the ratio of Graphene NanoFlake (GNF) and PEDOT-PSS in DMSO (Dimethyl Sulfoxide) solvent. Our results show that Whatman filter paper serves as a porous substrate for stable impregnation of conductive and functionalized ink for electrochemical immunoassays. We coated paper-based substrates multiple times to improve the stability of the coatings. Using brief UV Ozone or atmospheric plasma-based dry oxidation, we increased the number of active sites on the sensor surface for TNF- α antibody attachment via EDC-NHS chemistry. The resultant sensor was able to detect biomolecules such as cytokines in pg/mL range and in complex environments such as human serum.

Background Study of Shear Exfoliated 2D Nanocomposites

Elastomers are thermoset type of polymers, which are highly viscoelastic in nature, that are formed by combining precursors, including the elastomer monomer, and curing agent, to induce polymerization and curing. Elastomers and rubber-based composites with conductive fillers provide several advantages compared to conventional rigid sensors. Conductive elastomeric polymer and rubber-based composites are capable of withstanding large strain in multiple directions, are biocompatible, lightweight, consume low power, and can be stretchable, flexible, and therefore wearable (Amjadi et al., 2016; Li et al., 2012; Lu et al., 2019). Due to these unique properties, these sensors can be incorporated into clothes, gloves, garments, and even directly on the skin (Yamada et al., 2011).

Elastomers with different fillers such as graphite (flake or powder), graphene, carbon nanotube (CNT), and carbon black (CB) have been employed to fabricate sensors with different

techniques. For example, Figueira *et al.* fabricated Polydimethylsiloxane (PDMS)/Graphite flake composites (40%, 45%, 50% wt. ratio) by simply mixing them with a curing agent as capacitive touch sensors (Figueira et al., 2022). PDMS/CNT composites were also developed using ultrasonication and pouring in a frame/template, and this sensor was then employed to sense different human motions such as finger/elbow joint/wrist/knee bending, drinking, and walking (Liu et al., 2022). Based on room-temperature-vulcanized (RTV) silicone rubber reinforced with CNT, nanographite (GR), and CNT-GR hybrids, a flexible strain sensor, and actuator was fabricated using solution mixing by Kumar *et al.* (Kumar et al., 2021). Kurian *et al.* fabricated Ecoflex-00-30 with a graphite flake flexible sensor which showed the potential of electrothermal devices (flexible protective circuits and flexible temperature sensors) (Kurian et al., 2020). Another flexible Ecoflex-CNT composite was developed by Amjadi *et al.* and they performed human skin motion detection (finger, wrist, elbow, and multiaxial skin strain) (Amjadi et al., 2015).

Among different conductive fillers, graphene (single, few, and multi-layer) and exfoliated graphite are of great interest due to their exceptional mechanical properties (Jang et al., 2016), thermal and electrical conductivities, stability, and large surface area (Papageorgiou et al., 2015; Sadasivuni et al., 2014). This class of graphene-enhanced elastomeric composite, henceforth referred to as G-EMC, depends on the unique properties of both graphene/graphite and elastomer/rubber to sense its environment. Under external load, the distance between graphene in the composite and the structure of the hexagonal honeycomb will change, resulting in a change in the resistance of the composite sensor (Y. Wang et al., 2014). Elastomeric materials are insulating in nature, thus when graphene is added at lower concentrations, the nanoparticles are unable to form a continuous route, which results in poor electrical conductivity in the composites

(Araby et al., 2014). Electrons tunnel or hop from one graphene flake to another (if the filler content is above the percolation threshold in the composite), and that is why the change in distance between graphene flakes changes the resistance to electron flow (Sadasivuni et al., 2014).

Over the last decade, many researchers have shown the multifunctionality of this type of sensor. However, methods utilized to produce graphene are multi-step, expensive, and have the potential to include impurities during fabrication and transfer to the target polymer matrix (Jang et al., 2016). Moreover, the mixing of defect-free and inert pristine graphene with elastomers and rubber is inhomogeneous and leads to agglomeration in the matrix (Papageorgiou et al., 2015; Tang et al., 2014). Therefore, elastomers and rubbers like Polydimethylsiloxane (PDMS), Ecoflex and dragon-skin (platinum-catalyzed silicone), and polyisoprene are usually mixed with functionalized nanofillers using several techniques, including melt processing, in-situ polymerization, and solution blending to fabricate G-EMC (Papageorgiou et al., 2015). Among these methods, melt processing shows the most potential for commercialization with certain limitations (poor dispersion, material degradation) (Papageorgiou et al., 2015). All these limitations hinder the commercialization of G-EMC sensors.

In our method, a layered material (or combination of layered materials) graphite is exfoliated directly within one or both of the precursors of the elastomer, the elastomer monomer and/or curing agent, to shear the layers into graphene 2D nanoparticles (with a various number of layers in the c-axis direction) directly within the precursors using a batch mixer that imparts uniform, high shear, and after subsequent mixing and curing of the filled precursors, an elastomer nanocomposite with 2D nanoparticle enhancement results with improved mechanical, electrical, and thermal properties. The uniform mixing of fillers directly within the polymer was

verified by morphological characterizations (Lynch-Branzoi et al., 2020) and a non-destructive thermography approach (Ashraf et al., 2020; Rahman, Becerril, et al., 2022; Rahman et al., 2023) These flexible, conductive elastomeric nanocomposites are employed in various commercial applications, including sensors for detecting pulse, blood pressure, temperature, small movements, or deflection as a strain sensor (i.e., finger wag), tactile sensor, etc.

CHAPTER II

2D NANOMATERIAL AND NANOCOMPOSITE BASED SENSING DEVICES

Strain or Electromechanical Sensing

Nanofiber-Based Sensing

Materials. KYNAR 741 polyvinylidene fluoride (PVDF) powder was obtained from Arkema Inc. Dimethylacetamide (DMA, $\text{CH}_3\text{CN}(\text{CH}_3)_2$) and aniline ($\text{C}_6\text{H}_5\text{NH}_2$) were acquired from Sigma-Aldrich. Acetone ($(\text{CH}_3)_2\text{CO}$) and ethanol ($\text{C}_2\text{H}_5\text{OH}$) were purchased from Fisher Scientific. Ammonium peroxydisulfate (APS, $(\text{NH}_4)_2\text{S}_2\text{O}_8$) was purchased from Alfa Aesar. Hydrochloric acid (HCl) was bought from Acros Organics.

Preparation of PVDF/PAni Fiber Mats. A polymer solution was prepared by adding a 1:1 ratio of DMA and acetone with PVDF powder. The solution was then fed into the spinneret of a Cyclone system (Fiberio Technology Corporation) and spun at 8000 rpm the developed nonwoven fiber mats were collected in vertical posts surrounding the spinneret. To coat the PVDF fibers with polyaniline, at first, 0.1M APS was added into 1M HCL solution. A PVDF fiber mat was submerged into the solution. 2ml aniline monomer was dropped carefully onto the fiber to cover the whole mat. The whole solution was then covered completely with aluminum foil and left in an orbital shaker for 3 hours to facilitate the polymerization process. After turning off the orbital shaker, fiber with the solution was left for 48 hours for proper polymerization. Later, the dark green fiber was washed with 0.1M HCl, distilled water, and ethanol to get rid of any residue. Finally, the fibers were dried overnight at room temperature. This in-situ

polymerization of polyaniline on PVDF (PVDF/PAni) fiber mat was achieved by using a modified procedure described by Singh *et al* (Singh et al., 2008).

Electrical Characterization. A rectangular sample size of 20 x 9.5 mm² with a thickness of 0.4318 mm was sandwiched between two copper electrodes to evaluate the electrical properties of PVDF/PAni nanofibers. The I-V characteristics (Volume Resistivity) were determined using the Keithley 2450 Source Meter Unit (SMU) and ASTM D4496 - Standard Test Method for D-C Resistance or Conductance of Moderately Conductive Materials.

Temperature Test. The PVDF-PAni (both coated and uncoated) samples were heated with a hot air gun, and the temperature was measured in real time with a Fluke RSE 600 Infrared (IR) Camera. The IR camera and the BK Precision 5491B Multimeter were connected to a computer to obtain temperature and resistance data, respectively.

Drop Casting of Graphene on PVDF/PAni. A homogenizer (Benchmark Scientific-D1000) was used to mix 0.01 g of graphene nanoplatelets (surface area of 750 m²/g, supplied by Sigma Aldrich) with 10 ml of isopropyl alcohol and acetone (0.1% w/v solution) for 5 minutes at different speeds. A 2 ml volume solution was then drop-cast on two separate PVDF/PAni nanofiber samples (10x10 mm²) using a micro pipet. The coated sample was kept at ambient conditions for about 1 hour to dry out the solvents. Then using copper tape, electrodes on both surfaces were made, and the PVDF/PAni sample was incorporated with a polydimethylsiloxane (PDMS) (Sylgard 184, Dow Chemicals) as a protective layer. For the rest of this manuscript, the graphene-IPA and graphene-acetone drop cast samples are labeled as G@PVDF/PAni (IPA) and G@PVDF/PAni respectively.

Characterization. Scanning Electron Microscopy (SEM) images of PVDF/PAni and G@PVDF/PANI are shown in Figure 2. PVDF/PAni fiber nanofibers are characterized by fibrous structure, and coarse surface in Figure 2(a). Better visibility at higher magnification (10000x) revealed that PAni coated the PVDF nanofibers uniformly (Figure 2b). In comparison to the PVDF/PAni nanofiber, a significant amount of PAni densification can be seen in the G@PVDF/PAni SEM image (Figure 2c-d). Additionally, Figure 2c-d show that graphene flake is well attached to PAni coated PVDF nanofibers (yellow circles). To attach graphene to the fibers, we used acetone to mildly dissolve PVDF/PAni nanofiber structure. Graphene nanoflakes in acetone then get embedded into the nanofiber upon evaporation of the solvent. Due to this reason, some PAni is removed from the fiber and gets deposited as the densified layer next to the fiber. Figure 3 shows the XRD patterns of PVDF/PAni and G@PVDF/PAni nanofiber composite membranes. PVDF crystallizes primarily in the α -phase with distinct peaks at 18.5° and 20.1° . PVDF transforms from α -phase to β -phase as the α -phase shows a metastable form, and the formation of the stable form (β -phase) is accomplished through the rearrangement of the PVDF molecule. The characteristic β -phase is observed at $2\theta \sim 20.7^\circ$ with both G@PVDF/PAni and PVDF/PAni, as shown in Figure 3. The strong peak at $2\theta = 14.0^\circ$ indicates a high [Cl]/[N] ratio, demonstrating that the PVDF/PAni nanofibers in the composite membranes are highly doped with HCl (Subramania & Devi, 2008). G@PVDF/PAni has a characteristic peak in the XRD pattern around $2\theta \sim 27.8^\circ$, indicating that it has a graphitic carbon-based material composition. The peak around $2\theta \sim 27.8^\circ$ (green vertical line) is more intense in G@PVDF/PAni sample compared to PVDF/PAni fiber mat. This demonstrated that this facile drop-casting process effectively attached graphene to PVDF/PAni fiber mat. Thermal stability of materials can be determined using thermogravimetric analysis (TGA). We performed the TGA in two separate

10x10 mm² samples with a heating rate of 10 °C/min in N₂ gas flow rate of 20 mL/min. RI (100 °C) is associated with water evaporation, RII (100-360 °C) with the decomposition of oxygen-containing groups, and RIII (360-600 °C) with carbon combustion (Farivar et al., 2021). The onset degradation temperature of the polymer chain for PVDF/PAni is around 420 °C, whereas for G@PVDF/PAni is 410 °C (Figure 3b). This can be attributed to the higher carbon nanomaterial combustion. G@PVDF/PAni losses its mass due to drop-casting of graphene-acetone solution which etched away some of the polymer bonds and hence graphene-coated sample degraded at a higher rate than the normal PVDF/PAni fiber mat.

Resistivity test using ASTM D4496. The standard test method ASTM D4496 is attributed to DC resistance or conductance of moderately conductive materials. The I-V characteristic plot is obtained from Keithley 2450 SMU. The linear relationship between the current and voltage is shown in Figure 4. Volumes resistivity (current passing through the body of the fiber mats meaning resistivity across the thickness, whereas surface resistance is the resistance along the surface of a material) determinations are often used in checking the uniformity to detect the impurities that affect the quality of the material. We determined the volume resistivity using the equation (1),

$$\rho_v = R_v \frac{A}{t} \quad \dots\dots\dots (1)$$

where A & t are electrode area and PVDF/PAni nanofiber mat thickness respectively, and R_v represent the inverse of the slope of the I-V plot. Volume resistivity calculated using the above equation (1) for PDVF/PAni and G@PVDF/PAni is 9.3×10^6 & 8.31×10^6 Ω-cm respectively. Therefore, the volume conductivity (opposite to the volume resistivity) for PVDF/PAni & G@PVDF/PAni are 1.08×10^{-7} & 1.2×10^{-7} S/cm.

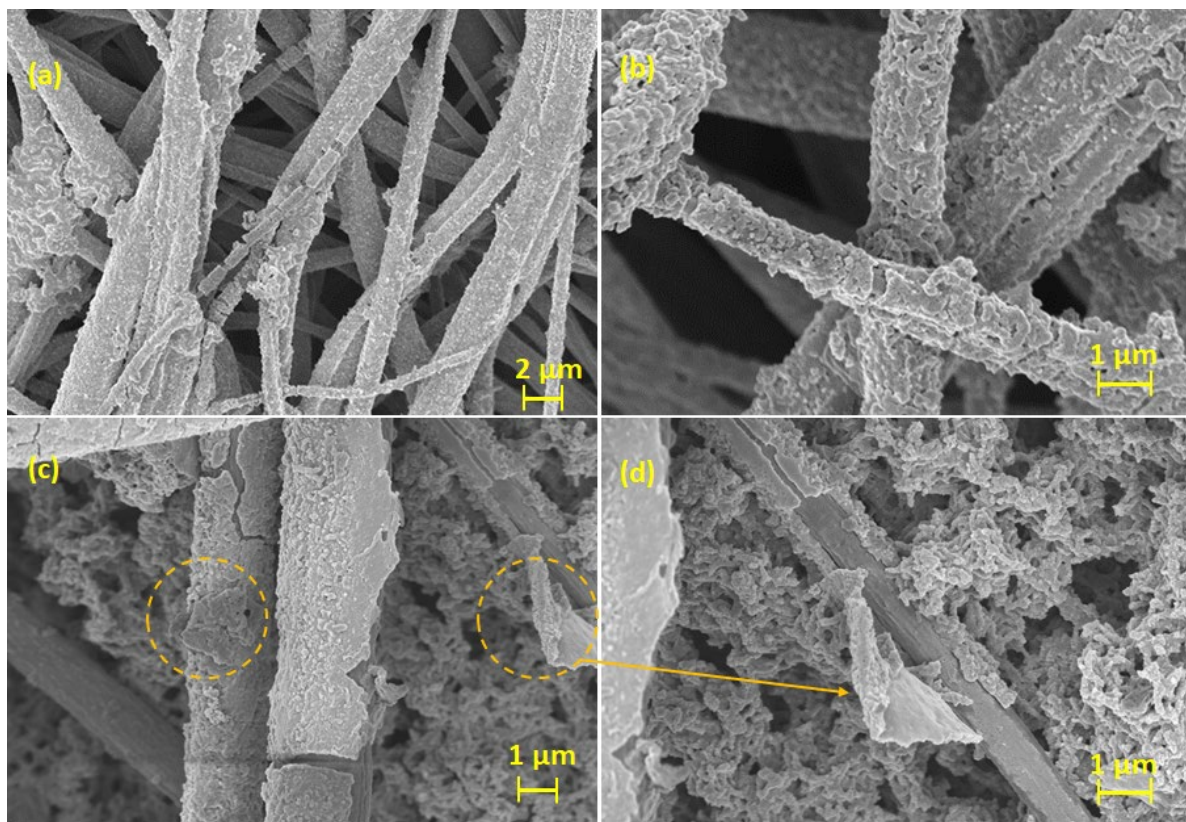


Figure 2: SEM images of PVDF/PAni fiber mat at a magnification of a) 3000x, b) 10000x. SEM images of G@GPVDF/PAni fiber mat at a magnification of c) 7710x, d) 10000x. Yellow dotted circles represent graphene flakes attached to the fibers.

From the I-V characteristics, the maximum current of PVDF/PAni fiber mat was around 6.5 μA at 9V which is about 4.5 times higher than what Chang *et al.* found at 9V (Chang & Hsu, 2013). This signifies the nanofiber sample can conduct a high current.

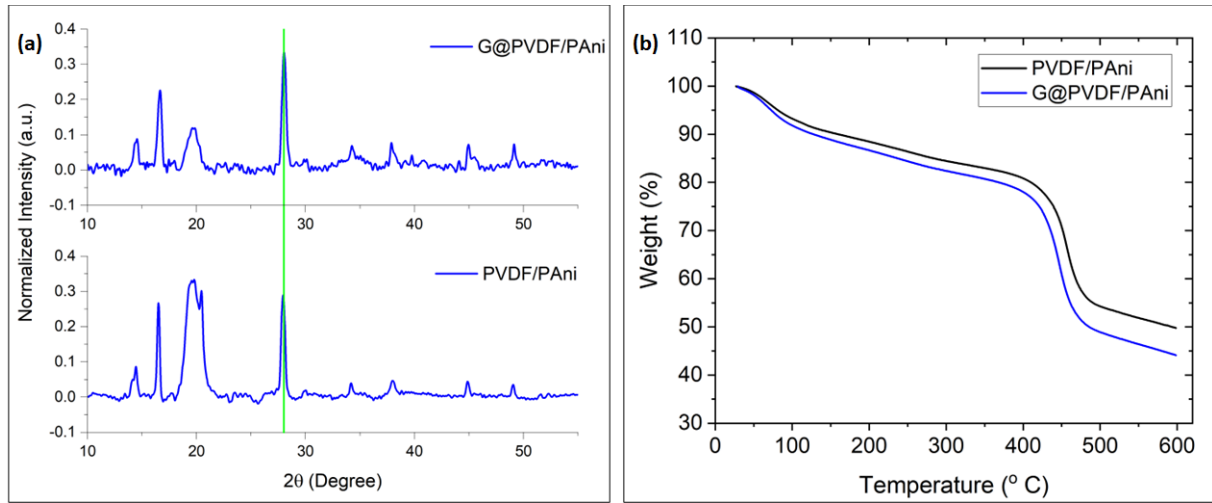


Figure 3: (a) X-Ray Diffraction (XRD) of G@PVDF/PAni and PVDF/PAni fiber mats. (b) Thermogravimetric analysis (TGA) of PVDF/PAni and G@PVDF/PAni.

Temperature Sensing. Fluorine and hydrogen atoms are located at the two sides of a carbon chain in a polarized PVDF fiber. So, under a stable environment, negative or positive charges induced perpendicular to the film's surface are constant. But this equilibrium can be broken if the temperature of the PVDF/PAni film is changed (pyroelectric effect) (Ueberschlag, 2001). A Fluke RSE600 IR camera (Figure 5a) was employed to measure the temperature, and the mean temperature of the sample area was calculated using SmartView R&D and MATLAB software. Resistance decreases of PVDF/PAni when temperature increases (from room temperature 28 °C to 70 °C) as more screen charges (surface charges) are released. The resistance changes for G@PVDF/PAni and PVDF/PAni increased to 28% and 22% respectively at the maximum temperature of ~70 °C (Figure 5b-c). Furthermore, the resistance changes for G@PVDF/PAni and PVDF/PAni followed different trends with G@PVDF/PAni showing higher sensitivity.

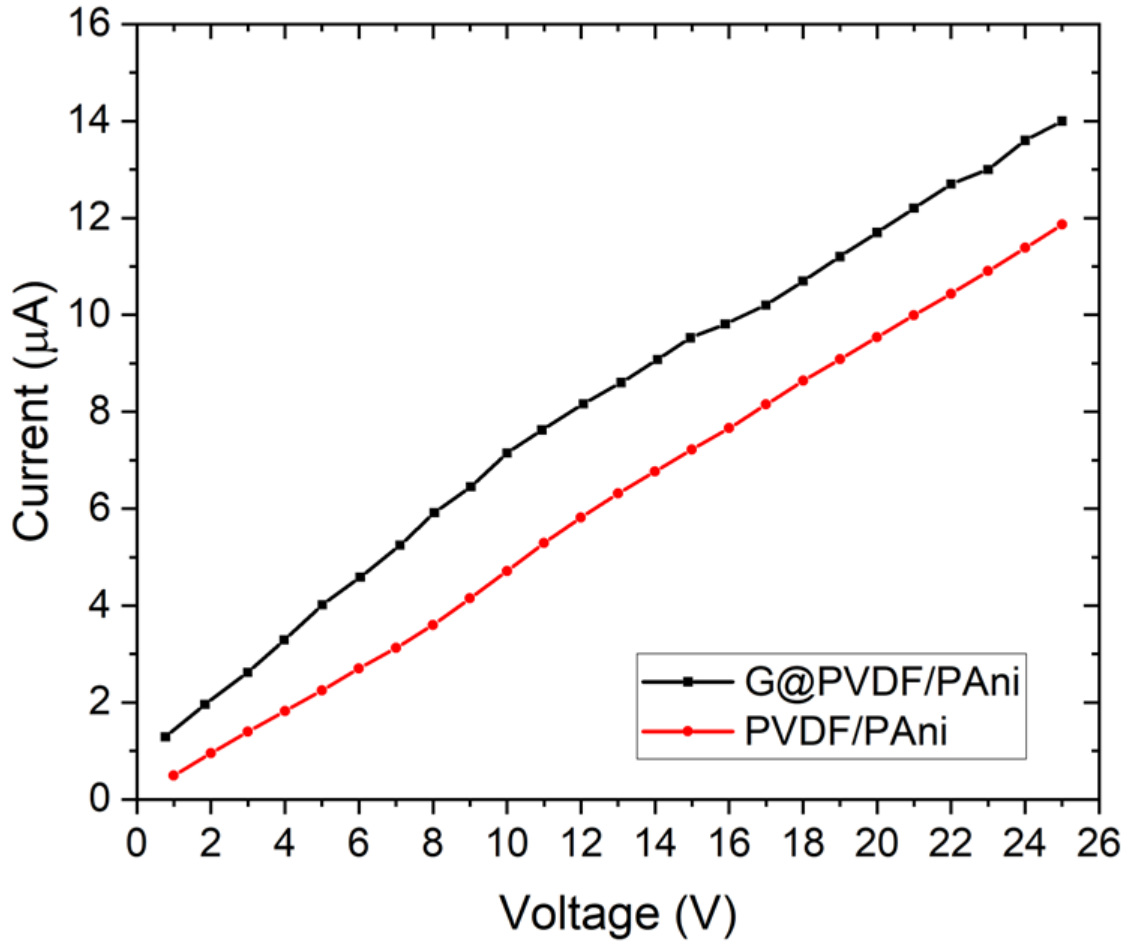


Figure 4: Current-Voltage (I-V) characteristics of the conductive PVDF/PAni and G@PVDF/PAni.

Finger Tap-in. In a piezoelectric material, a simple finger tap can induce voltage and current signals. When mechanical stresses in the form of pressure are applied to a piezoelectric film, surface charges are released and moved toward the copper electrodes (positive signal-induced). When the stress is released, charges flow back in the opposite direction, hence producing a negative voltage signal. Compared with the pure force spin PVDF/PAni fiber, the conductivity of G@PVDF/PAni was significantly higher due to the atomic interaction between PVDF/PAni and graphene atom (Y. Wu et al., 2012; Zhang et al., 2012). Graphene had a positive

effect on forming a more conductive network, and it also enhanced the mechanical properties. The structure of the PENG consists of a piece of PVDF/PAni fiber sandwiched between two copper foil electrodes and PDMS. Figure 6a-d presented the open-circuit voltage and short-circuit current of PVDF/PAni nanocomposite. The signals were achieved under the random finger press. The G@PVDF/PAni (IPA) nanocomposite had a better voltage and current signal than the pure PVDF/PAni fiber. Because treating the films with acetone or methanol and inclusion of graphene increases conductivity(Kinlen et al., 1998), graphene with acetone solution increased the conductivity of the fiber mat. The short circuit current achieved was 14 mA pk-to-pk compared to 700 nA of 2 % rGO/PVDF sample experimented by Yang, J., et al(Yang et al., 2021).

Moreover, at the same graphene content, the G@PVDF/PAni induced a maximum voltage of around 75 mV pk-to-pk (Figure 7a) as compared to 27 mV pk-to-pk from G@PVDF/PAni (IPA) nanocomposite. Therefore, G@PVDF/PAni prepared using acetone showed better performance than PVDF/PAni and G@PVDF/PAni (IPA) in terms of voltage generation.

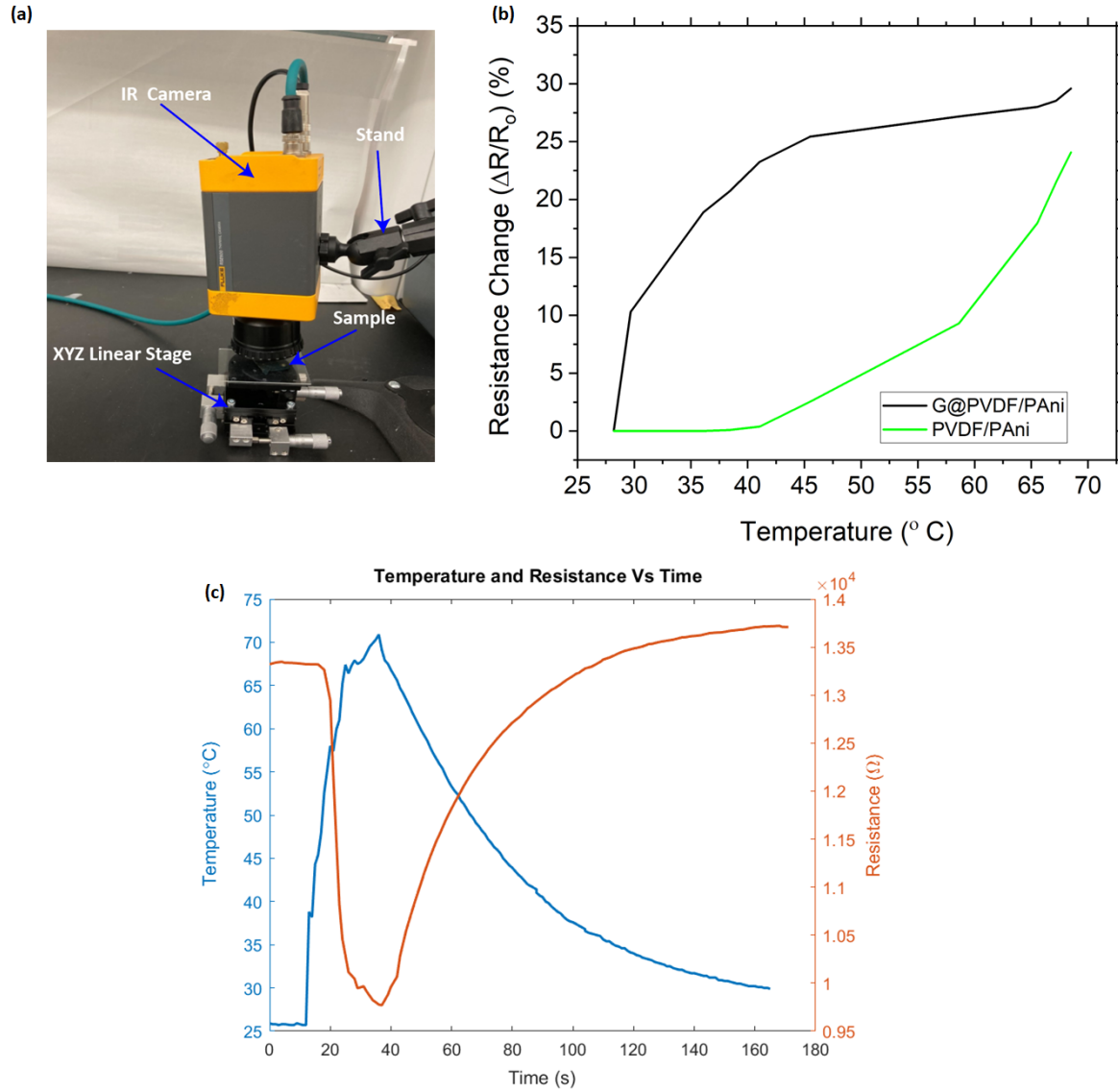


Figure 5: (a) Temperature sensing setup having Fluke RSE 600 thermal camera, close-up lens, and XYZ stage, (b) Temperature change of G@PVDF/PAni and PVDF/PAni with temperature. The sample was heated by a heat gun and resistance was recorded using a BK precision multimeter, (c) Temperature and Resistance change with time.

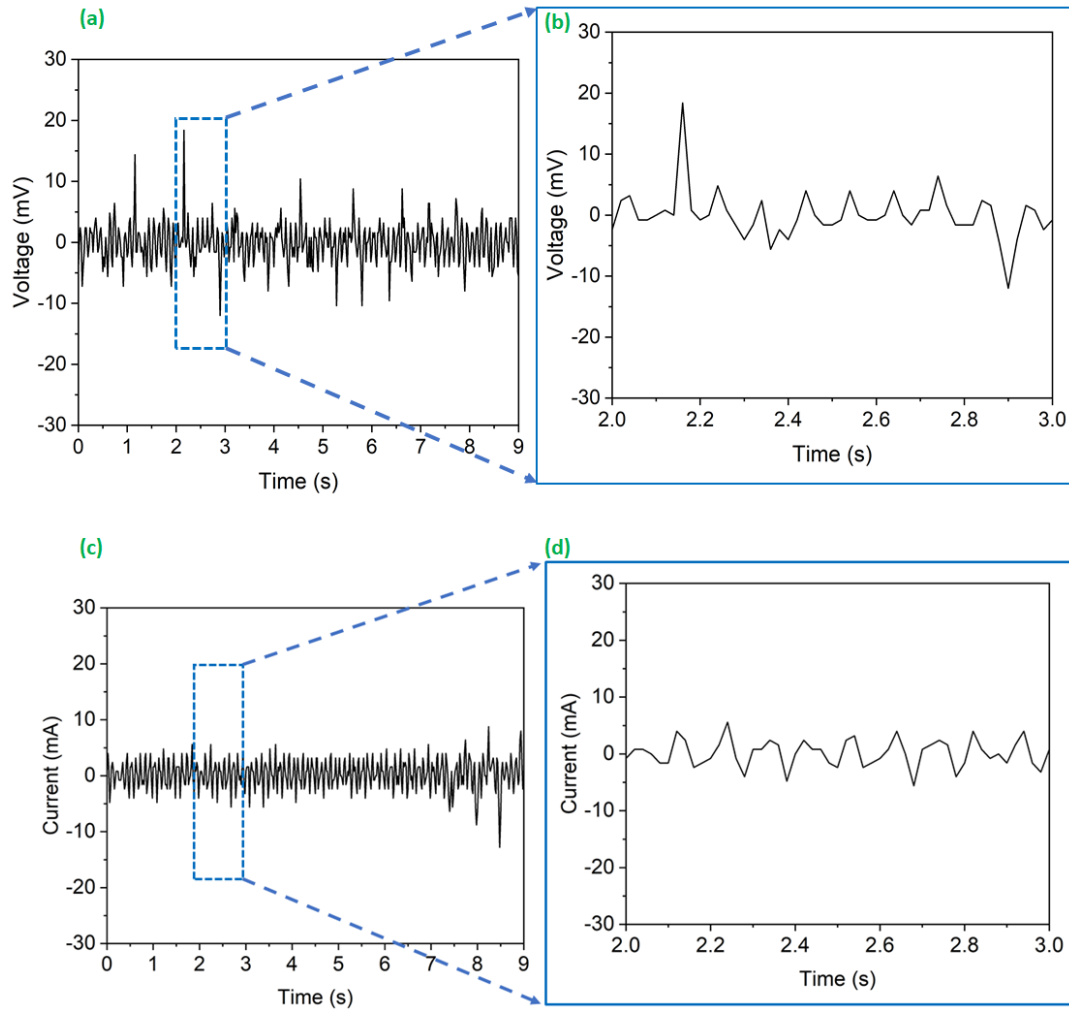


Figure 6: (a) Open-circuit voltage (V_{OC}) of PVDF/PAni nanofiber under finger pressing condition, (b) Open-circuit voltage (V_{OC}) signal during the time from 2 to 3 seconds, (c) Short-circuit current (I_{SC}) of PVDF/PAni PENG under finger pressing condition, (d) Short-circuit current (I_{SC}) signal during the time from 2 to 3 second.

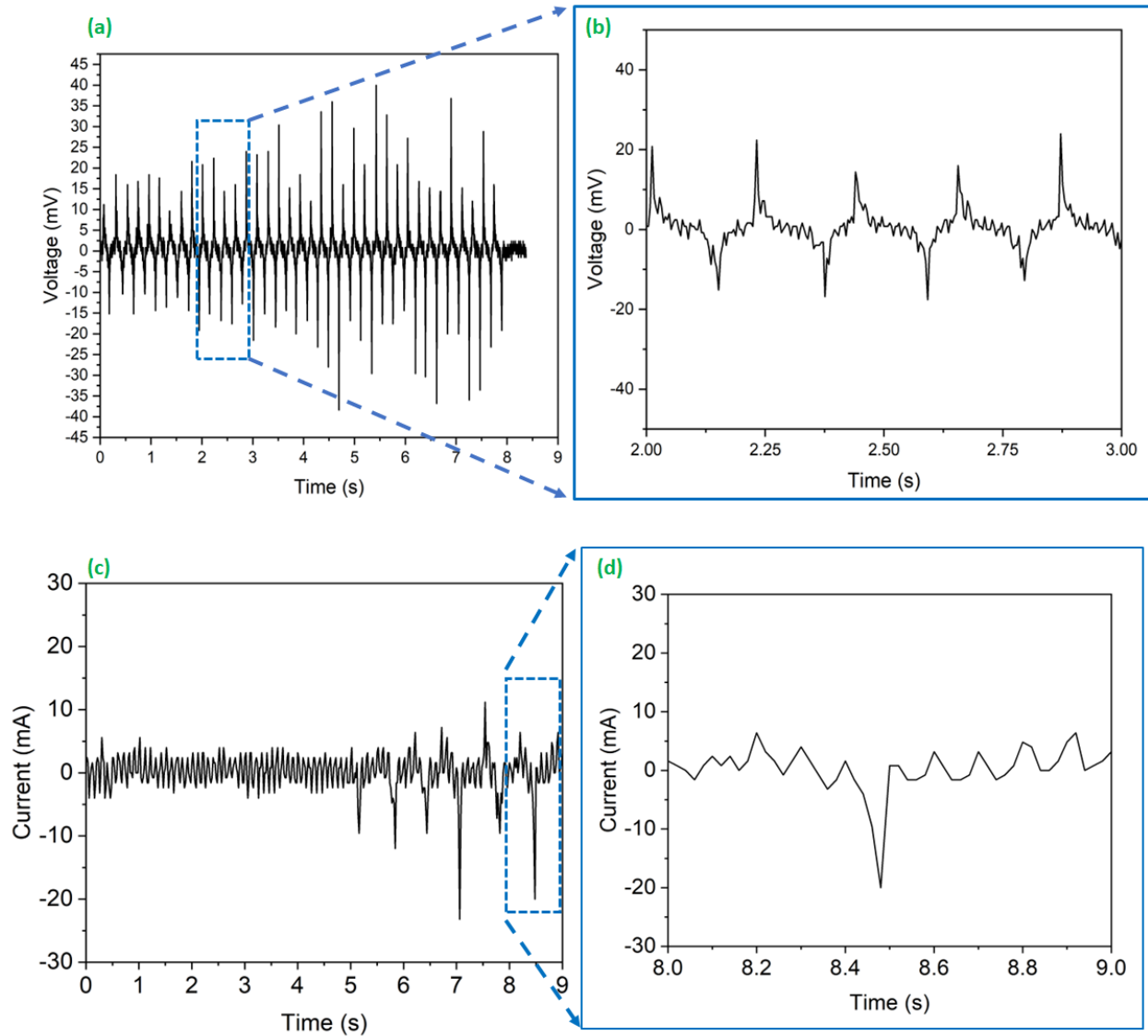


Figure 7: (a) Open-circuit voltage (V_{OC}) of G@PVDF/PAni under finger pressing condition, (b) Open-circuit voltage (V_{OC}) generation during the time from 2 to 3 seconds, (c) Short-circuit current (I_{SC}) of G@PVDF/PAni (Acetone) under finger pressing condition, (d) Short-circuit current (I_{SC}) signal for 1 second (enlarged view).

In-Situ Shear Exfoliated Graphene Nanocomposites for Sensing

Methods. Ecoflex-00-30 Part A and Ecoflex-00-30 Part B with 35-40% Graphite were mixed in a Hauschild planetary shear mixer at 2500 rpm for 2 minutes to get a homogenous mixing. Using shear exfoliation, graphite was converted into graphene nanoflakes (GNFs) directly within a silicone polymer precursor (Ecoflex-00-30 Part A) and curing agent (Ecoflex-00-30 Part B) separately in a Randcastle batch mixer for 3-10 minutes at 100 rpm. The filled polymer precursor (G+Ecoflex-A) was then combined and mixed with the filled curing agent (G+Ecoflex-B) component and allowed to cure, according to the manufacturer's curing conditions (1 part polymer precursor to 1 part of curing agent by weight). The schematic of shear exfoliation of graphite in a batch mixer is given in Figure 8a. With increasing mixing time, the degree of graphite exfoliation into GNFs increases, and the distribution of the number of layers in the GNFs decreases. The GNF-matrix interaction is very strong since each newly exfoliated GNF has a pristine surface, and fracturing across the AB Basal plane of the GNFs provides reactive sites with the potential for primary covalent bonding between GNF edges and the surrounding medium (either the polymer precursor or the curing agent) thereby providing in situ functionalization. G-EMC sensors (size of $25 \times 10 \times 1.5 \text{ mm}^3$) fabricated from polymers prepared in this fashion were tested for their applicability to health monitoring and temperature sensing. G-EMC sensor was attached to different human body parts and using a Keithley 2500 sourcemeter resistance/current was measured at a maximum voltage of 5V. For temperature sensing, a heat gun was used to heat the sample in the middle, and using Fluke RSE600 infrared (IR) thermal camera, real-time temperature was recorded. Later, the temperature data was analyzed via Smartview R&D, Matlab, Excel, and Origin Pro software packages. Three electrode configurations (working electrode: G-EMC of size $10 \times 10 \times 1.5 \text{ mm}^3$, counter electrode: Pt wire,

and reference electrode: Ag/AgCl) were chosen over two electrode configurations for electrochemical sensing because they are more accurate.

Characterization. Graphene is a unique material that has excellent mechanical, electrical, and thermal properties that made it possible to utilize it in different applications like sensors, and transistors. In order to study graphite/graphene-based devices or sensors, it is important to distinguish the number of layers that play a crucial role in the performance. Raman spectroscopy provides a reliable technique to determine the number of layers and some other properties in a carbon-based material. Raman spectra of 35 and 40 wt.% G-EMC sensor is shown in Figure 8b. G band (appears at $\sim 1580\text{ cm}^{-1}$) indicates the number of graphene layers, and it moves to lower frequencies as the number of layers increases. D band or the disorder band appeared at $\sim 1350\text{ cm}^{-1}$, and for 40 wt% G-EMC sensors, the D band peak intensity is higher than 35 wt% G-EMC. The 2D band appears at $\sim 2700\text{ cm}^{-1}$, and both 40 wt% G-EMC & 35 wt% G-EMC showed a similar 2D band intensity. The normalized intensity of the 2D band is 0.7 in comparison to the G band, indicating that few graphene layers were formed during graphene exfoliation. Scanning electron microscopy (SEM) images for 40 % wt. G-EMC was shown in Figure 8c-f at different magnification scales. These images indicate the graphene flakes and their shapes in different spatial locations.

I-V Characterization. I-V characteristics using source a meter (Keithley-2450) were carried out to measure the sensor's current at a certain voltage. Voltages varied linearly from 1V to 20 V. The current-voltage (I-V) relationship followed almost a linear profile shown in Figure 9a and the conductivity of the G-EMC was 20.59 S/m.

Finger and Elbow Bend Detection. G-EMC sensor was attached to the finger to detect its signal during different finger bends. When the finger was straight (0°), it showed a constant

resistance ($\sim 55 \Omega$) (Figure 9b). The finger bending angle (0° , 30° , 45° , 90°) changed after every 10 seconds, and the sensor reached a maximum immediately after changing the angle (response time ~ 400 ms). After that, resistance starts to decrease and reaches almost a constant value for every bending angle. As the bending angle was getting larger, the peak resistance increases due to mobility between graphene flakes. Similar trends were obtained for elbow bending at different angles (0° , 30° , 45° , 90°) (Figure 9c).

Pulse, Breathing & Speech Detection. The G-EMC sensor was attached to the wrist for pulse detection, and the pulse can be easily detected by evaluating the sensor's resistance over time (Figure 10a). For one pulse cycle, the resistance raises to a maximum and then decreases to a minimum, through analyzing this maximum and minimum in a second, ones' pulse rate can be easily detected. Additionally, the sample was also tested near the nose for breathing detection and on the throat for speech detection. For breathing, the normalized current (for a certain voltage applied through the source meter) reached a peak during inhale and to a minimum during exhale (Figure 10b). For speech detection, the current depends on the sentence structure, individuals' speaking rate (words spoken per minute), and length. Furthermore, the sensor was tested with the same sentence of varying pause duration (small, large, and no pause), and it showed almost a similar trend each time (Figure 10c).

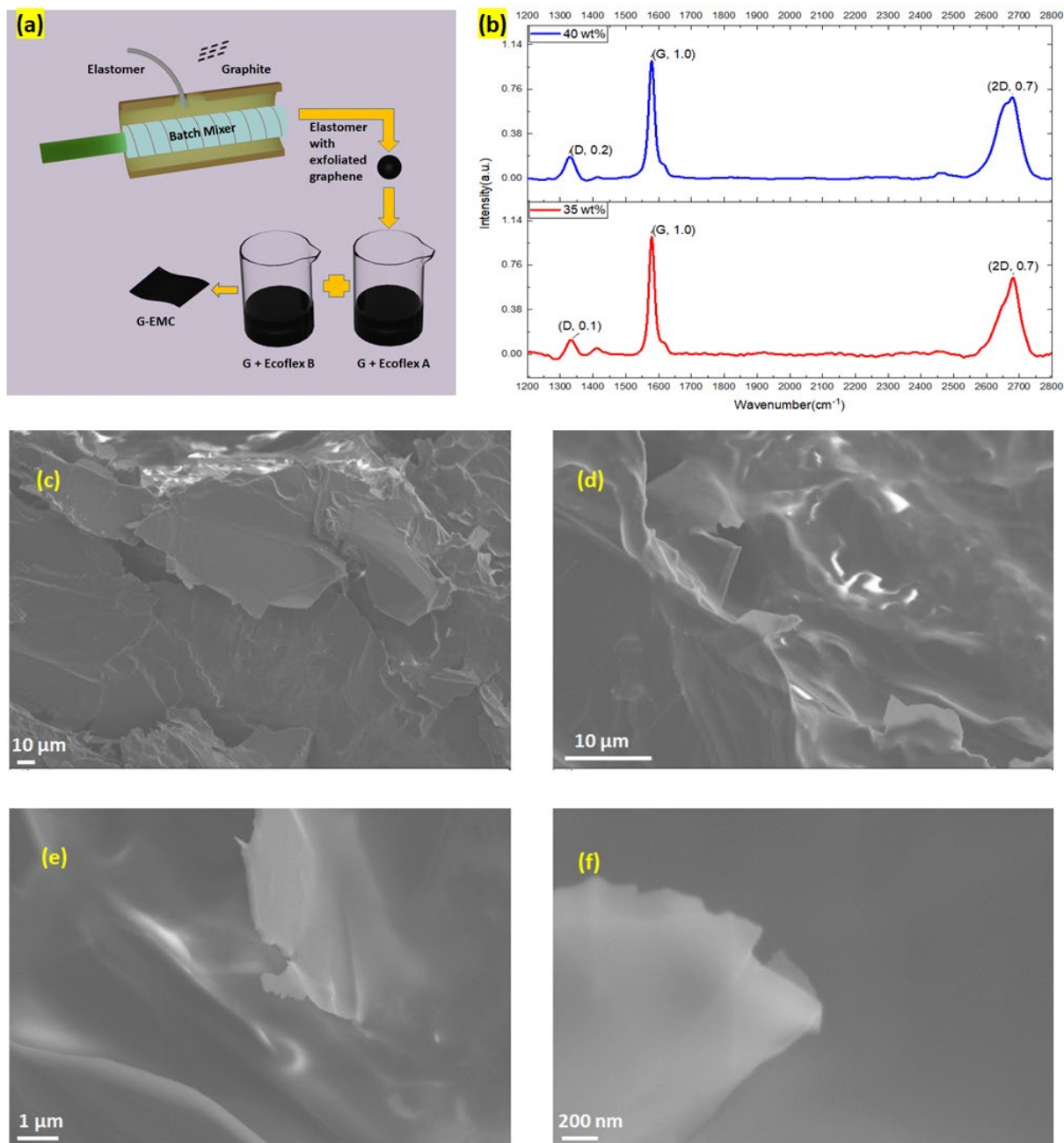


Figure 8: (a) Schematic of shear exfoliation of graphite and G-EMC fabrication in a batch mixer. (b) Raman spectra of 35 and 40 wt% G-EMC sensors, (c-f) SEM image of 40 wt% G-EMC sensors at different length scales.

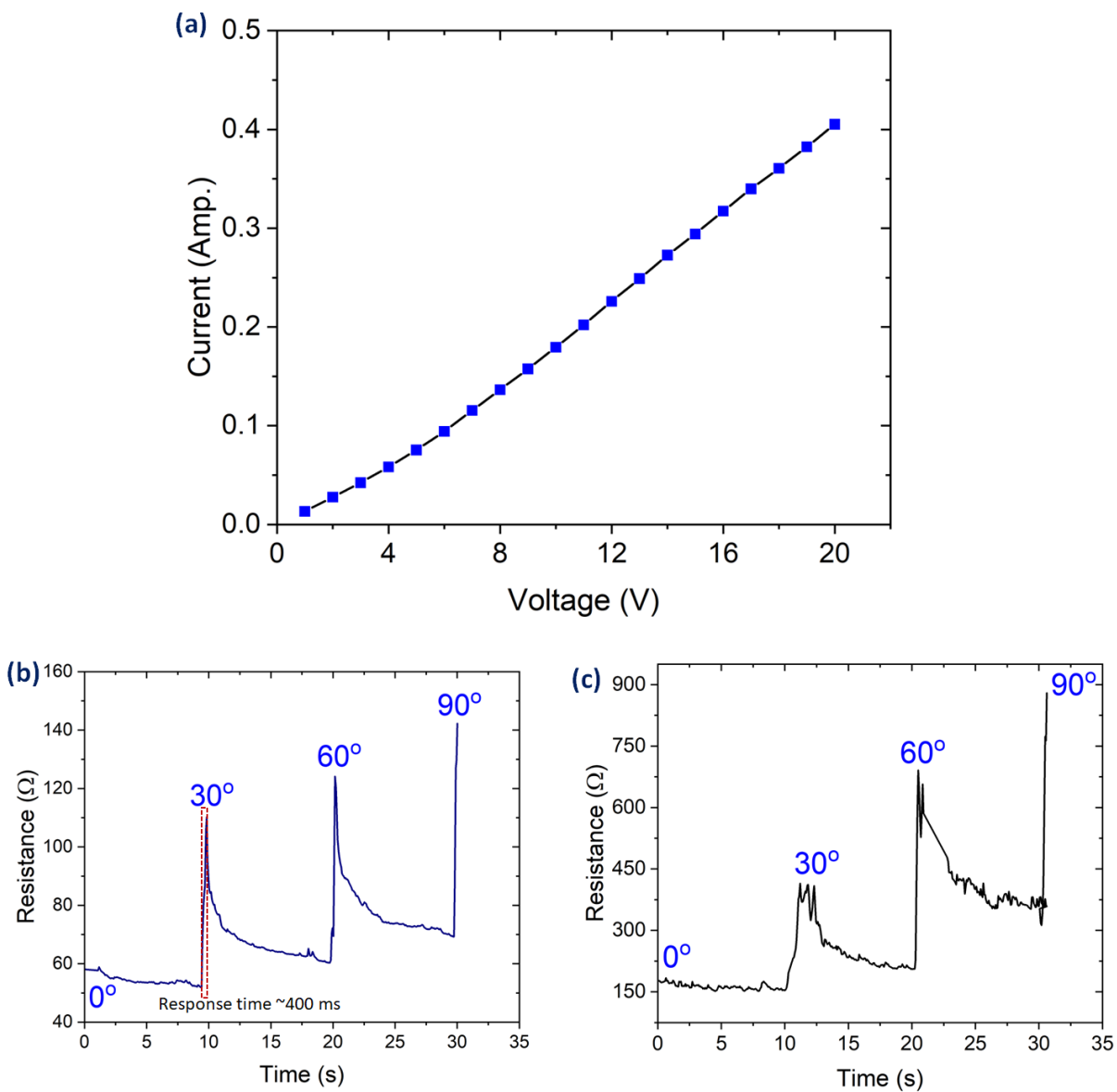


Figure 9: (a) I-V characteristics plot for 40 wt. % G-EMC sensor, (b) Finger bending (0°, 30°, 45°, 90°), and (c) Elbow bending (0°, 30°, 45°, 90°) detecting using the G-EMC sensor.

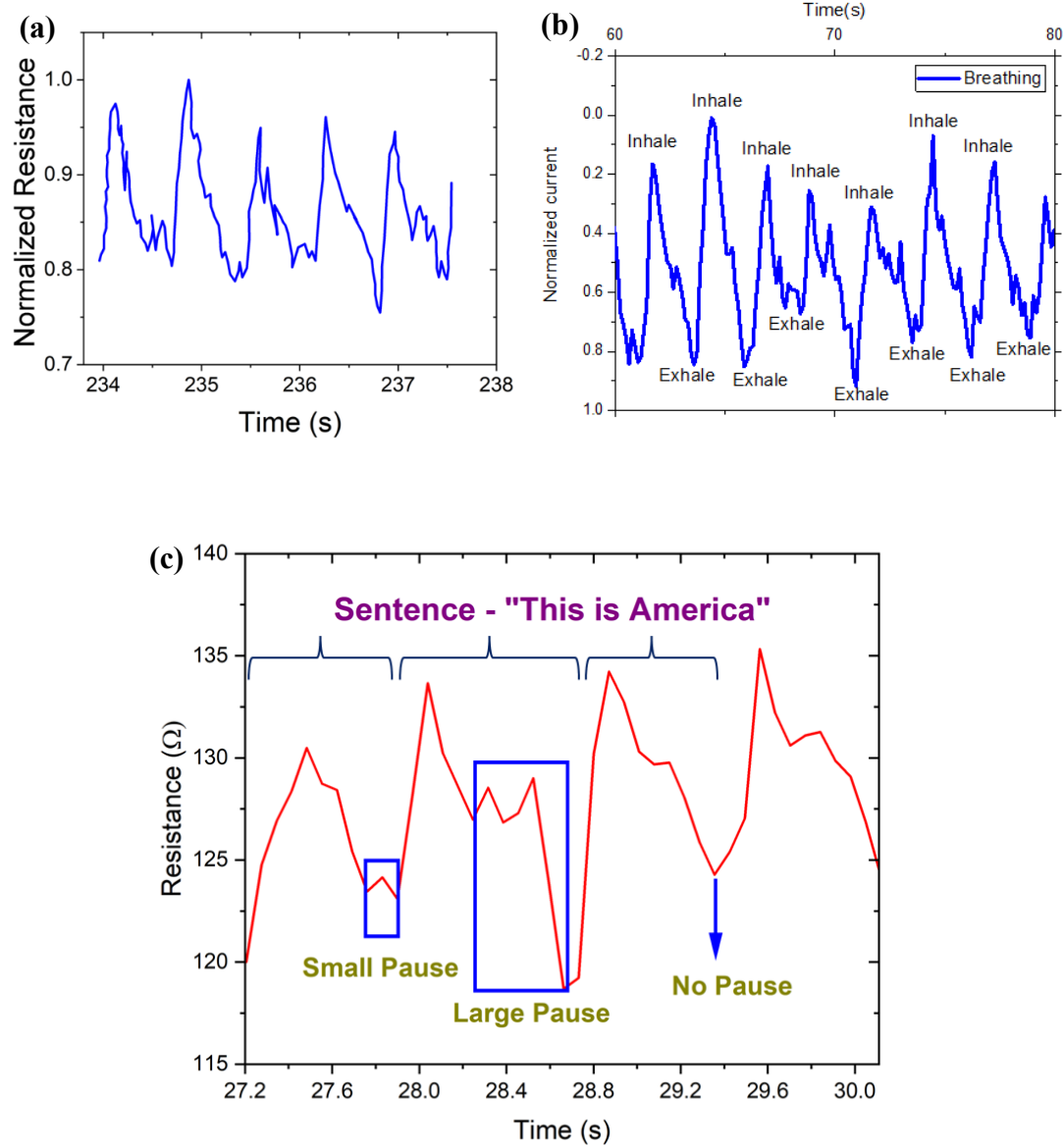


Figure 10: (a) Pulse, (b) Breathing, and (c) Speech detection using G-EMC sensor.

Paper Based Electrochemical Sensing for Biomolecules Detection

Sensor and Ink Preparation

Ink Preparation. 1 g of Graphene NanoFlake (GNF), 3 mL of PEDOT:PSS, 3 mL De-Ionized (DI) water and 800 μ L of DMSO solvent were added into a container (Figure 11a). The solution was then mixed uniformly using a Hauschild Planetary Speed Mixer with rpm 800 and 2500 each for 30 seconds.

Laser Cutting of Filter Paper and Electrode Dip Coating. Whatman® filter paper nos. 1 and 4 were used as a substrate for the electrodes. The process for making the electrodes is shown in Figure 11b. A specific CAD design (biosensor size: L= 13.7 mm, W = 7.2 mm, working electrode diameter = 3.7 mm) was made, and filter papers were cut via laser (Universal Laser System, PLS - 4.75). The counter electrode (C.E.) and the working electrode (W.E.) were dip-coated into the ink, and Ag ink was used for the reference electrode. These paper-based electrodes then dried out in the vacuum for 24 hours. For a stable connection, W.E. and C.E. contact pads were coated with Ag ink. To place the electrodes in a thick paper substrate, a double-sided scotch tape was used. After that, PDMS with a curing agent (10:1) was put in between the working zone and contact pads.

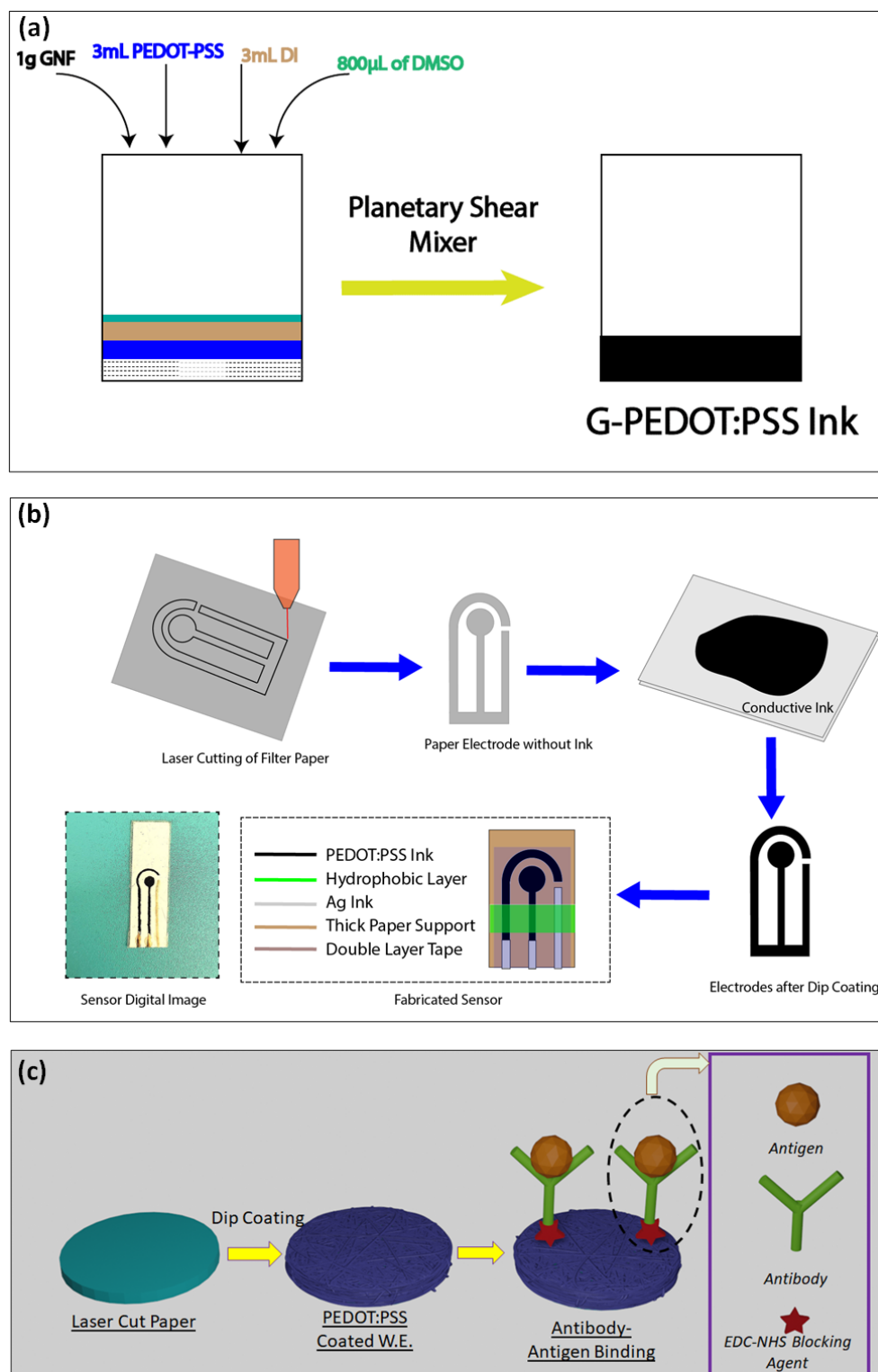


Figure 11: Schematic of (a) G-PEDOT:PSS conductive polymer ink preparation. (b) Paper-based biosensor fabrication. (c) Schematic representation of TNF- α /IL-6 detection protocol for paper-based electrodes.

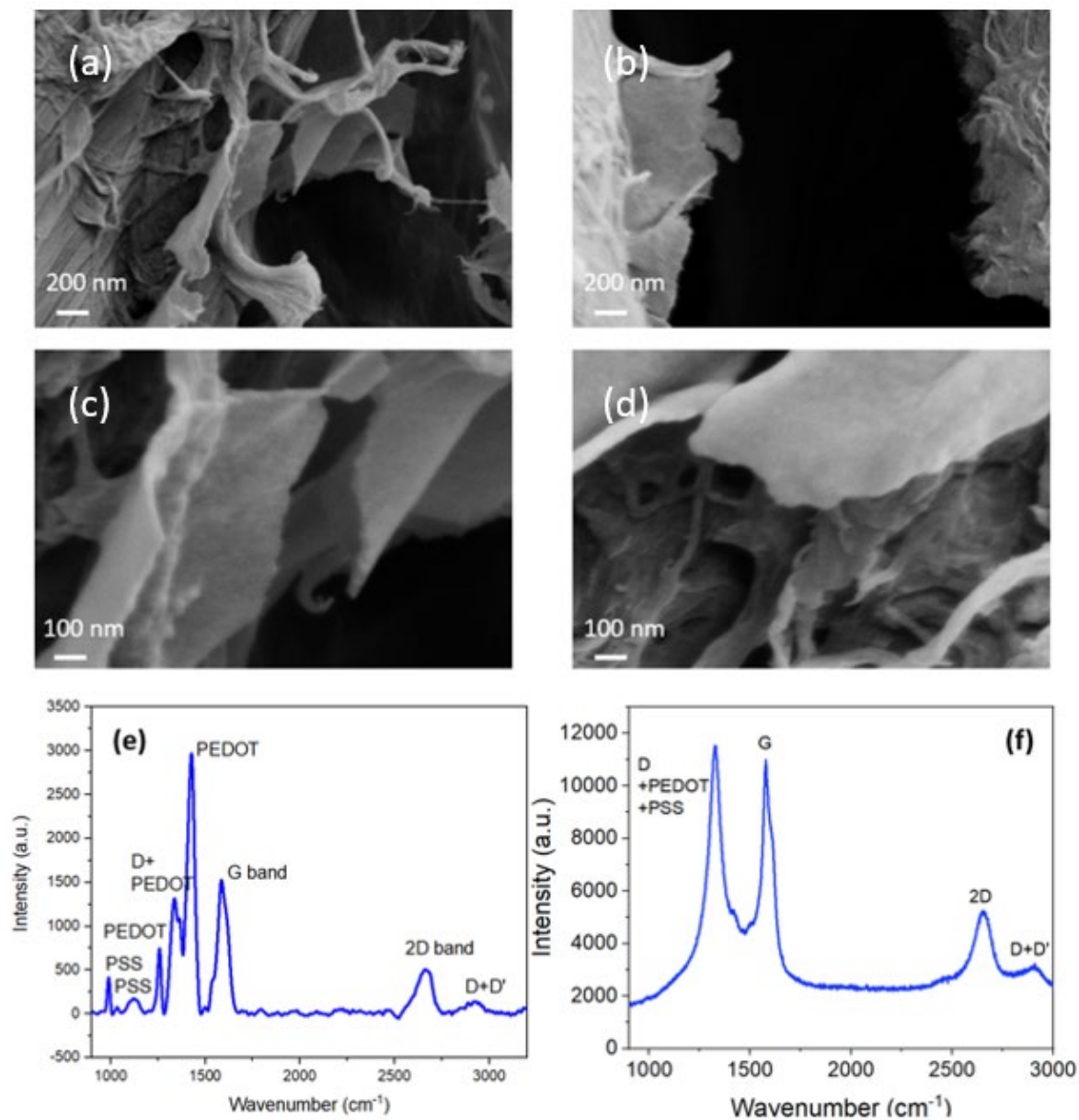


Figure 12: (a-d) Scanning electron microscopy images of GR-CP-paper-based sensor. Raman microscopy spectrum of the sensor (e) before oxidation and (f) after oxidation.

Dopamine Solution Preparation. Dopamine hydrochloride was mixed in PBS solvent and a range of dopamine concentrations from 12.5 μM to 800 μM was prepared by serial dilution method.

Surface Modification, EDC/NHS Conjugation, TNF- α Antigen, and IL-6 Antigen Solution Preparation. Initially, the G-PEDOT:PSS electrode surfaces were modified using a Novascan UV-Ozone instrument for 3 minutes (at 40 $^{\circ}\text{C}$) to form a carboxylic group (-COOH). Alternatively, similar oxygen functionalization can be obtained using mild oxygen plasma treatment. we performed mild dry plasma oxidation on the sensors at 150 mtorr for 10 seconds at 20 watts. Then, 0.4 M of EDC was added to the electrode working zone to couple with the -COOH groups and kept in a darker environment for 4 hours (Longo et al., 2016). Subsequently, 0.2 M NHS was used, and similarly, it was kept in dark for another 4 hours. After that, 20 μL of TNF- α Antibody/IL-6 was added to crosslink with the NHS and kept at 4 $^{\circ}\text{C}$ for 12 hours. Recombinant Human TNF- α (antigen)/IL-6 antigen solution of 5 pg/mL to 50 ng/mL was made using the serial dilution method. The detailed schematic of the TNF- α /IL-6 detection protocol is shown in Fig. 1c.

Scanning Electron Microscopy (SEM) and Raman Characterization. SEM characterization was carried out on the PEDOT:PSS paper-based biosensor (Zeiss, Germany). Raman spectroscopy, which can reveal signature peaks as well as the number of defects and functionalization from conductive polymers and graphene, was also used. We collected Raman data using a 633 nm laser using a Renishaw inVia reflex system with 50X magnification.

Electrochemical Analysis of Dopamine/TNF- α /IL-6. This paper-based sensor was connected with Autolab PGSTAT302N (from Metrohm) via an adapter. Cyclic Voltammetry (CV) and Electrochemical Impedance Spectroscopy (EIS) were performed to analyze our paper-based electrode sensors. A typical three-electrode method was chosen over the two-electrode method for accurate quantification. For dopamine, TNF- α detection, and IL-6 detection, we used 10 μ L of Ferrate (Fe^{2+}), 10 μ L of Ferric (Fe^{3+}) solution (both prepared using PBS solvent), and 2 μ L of dopamine/TNF- α antigen/ IL-6 antigen. In cyclic voltammetry (CV), a current is measured between the working electrode and counter electrode with the applied potential between the working and reference electrode. The parameters for cyclic voltammetry (CV) were: -0.5 V to 0.5 V with a scan rate of .05 V/s. The parameters for impedance spectroscopy were: start frequency - 10^6 Hz, stop frequency - .1 Hz, frequency type - logarithmic, frequency per decade - 10, and voltage - 10mV.

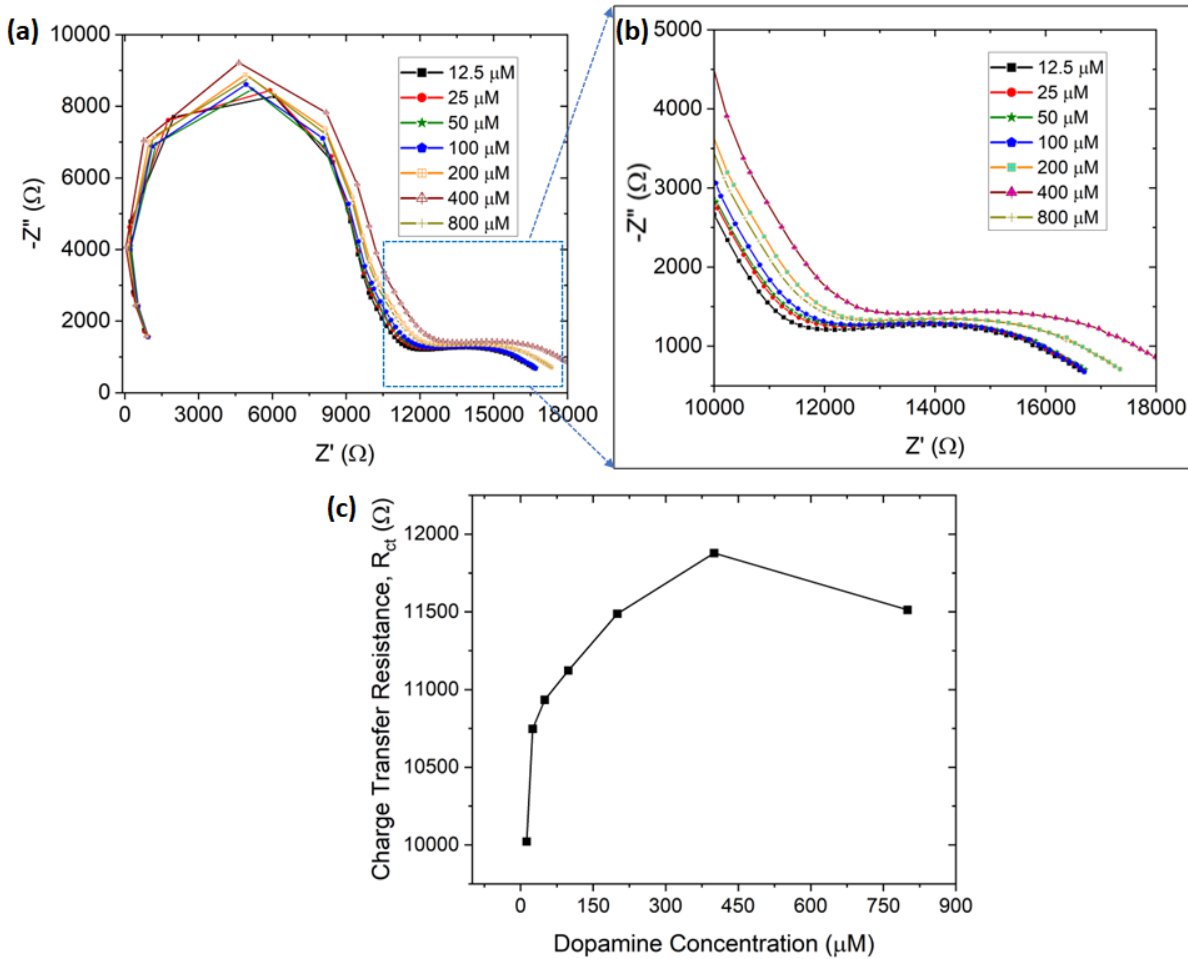


Figure 13: Single layer dip-coated paper-based biosensor (a) EIS characterization of dopamine detection from 12.5 μM to 800 μM , (b) Enlarged view of the tail in (a), (c) Charge Transfer Resistance plot with dopamine concentration.

Biomolecules Detection Using Paper Based Sensor

Characterization. The enhanced affinity of conductive polymer (CP) to cellulose fibers and interaction of CP with GNF allows GNF to be glued to the fibers. PEDOT:PSS self-assembles on the fibril in the wet stage and gets π -stacked after drying and, therefore, act as a glue to connect graphene with cellulose fibers (Ryu et al., 2017). This can be observed from the SEM images of the GNF-CP paper-based sensor in Figure 12a-d. The flat GNF sheets are connected to the fibrous structure of cellulose. The choice of ink components, mixing technique,

and substrate are critical for a stable and effective sensor. We used a Flacktek® mixer to achieve uniform mixing and introduce curvature to GNF. The Dual Asymmetric Centrifuge of the mixer ensures uniform mixing, and removal of bubbles, introduces curvature-induced strain to the GNF, and π - π^* interaction of GNF with PEDOT:PSS leading to enhancement of charge carrier concentration of GNF (doping) (Bogomolova et al., 2009; Paton et al., 2014; Voiry et al., 2016). We have also experimented with more viscous ink (containing double the amount of PEDOT:PSS compared to the original ink), which leads to the formation of a thick crust on the surface, preventing access to the micro-nano porous structure underneath.

Successful oxidation can be verified by Raman spectroscopy, which can show signature peaks from CP and graphene, and additionally, the number of defects and functionalization (D band). This mild oxidation treatment leads to broadening of the D peak ($\sim 1350\text{ cm}^{-1}$) as can be observed from before and after oxidation treatment in the Raman spectra (Figure 12e-f).

Dopamine Detection. The fabricated G-PEDOT:PSS paper-based sensor was employed to investigate the electrochemical characteristics of dopamine. EIS was used to investigate the conductivity and electron transport properties of single-layer and double-layer dip-coated electrodes. The charge-transfer resistance (R_{ct}) at the electrode surface depends on the total analytes on the electrode working zone. To verify our paper-based electrodes' reliability, 2 μL of PBS solution with 10 μL of each Fe^{2+} and Fe^{3+} was added to the working zone. After each dopamine concentration test, the electrodes were mildly washed using PBS solution and dried out for 30 mins. The charge transfer resistance (semi-circle diameter) is the same for the two similar runs and hence, it suggests our paper-based sensor can work reliably and repeatedly.

Nyquist plots (imaginary impedance vs. real impedance) are typically utilized to investigate interface properties. Usually, solution resistance, charge transfer resistance, double-

layer capacitance, and Warburg diffusion resistance can be derived from a Nyquist plot through mathematical modeling. The lower frequency corresponds to the diffusion-limited process and the high frequency represents the charge transfer resistance (Shao et al., 2010). The charge transfer resistance can be found from the diameter of the semicircle formed. EIS analysis of single-layer dip-coated (both counter and working electrodes are dip-coated with graphene-conductive ink, reference electrode is dip coated with Ag) electrodes for dopamine detection is shown in Figure 13a-b. The charge transfer resistance increases with the dopamine concentration from 12.5 μM to 400 μM due to more dopamine molecule adsorption on the surface (Figure 13c). Above 800 μM , the value for R_{ct} suggests maximum analyte molecule adsorption on the electrode surface. Figure 14a-b shows the Nyquist plot for double-layer dip-coated electrodes for the same dopamine concentration range, and Fig. 4c indicates the corresponding charge transfer resistance increasing with dopamine concentration from 12.5 μM to 400 μM . The R_{ct} values for double-layer dip-coated electrodes (4.75 $\text{k}\Omega$) were less than the single-layer dip coated (20.1 $\text{k}\Omega$), which indicates higher electrical conductivity for charge transport. The detection limit of dopamine can be calculated using the formula, $\text{LOD} = \frac{\sigma}{S}$ (σ is the standard deviation of the response and S is the slope = 0.13*(slope of semi-log plot)) (Hayashi et al.). LOD for dopamine detection was $\sim 3.4 \mu\text{M}$ using a calibration curve. Our paper-based sensors demonstrated similar or higher sensitivity and range for dopamine detection compared to prior work. For example, Yang *et al.* fabricated AuNPs@PANI nanocomposites to detect dopamine (range: 10-1700 μM , LOD: 5 μM) and ascorbic acid simultaneously (Yang et al., 2012). Gold nanoparticle on a polyaniline-modified electrode surface for the detection of dopamine (range: 20–100 μM , LOD: 16 μM) was fabricated by Mahalakshmi *et al* (Mahalakshmi & Sridevi, 2021). PEDOT:PSS organic electrochemical transistor (range: 5-100 μM , LOD: 6 μM) (Gualandi et al., 2016),

commercial screen-printed electrode modified by PEDOT:PSS/Chitosan/Graphene (range: 0.05-70 μM , LOD: 0.29 μM , more sensitive but with a smaller detection range) (Shen et al., 2020), and multi-walled carbon nanotube (MWCNT)-PEDOT (range: 10-330 μM , LOD: 10 μM) (Lin et al., 2010) sensors were the PEDOT based biosensors reported for dopamine detections. A comparison between prior reports and our work is presented in Table 1.

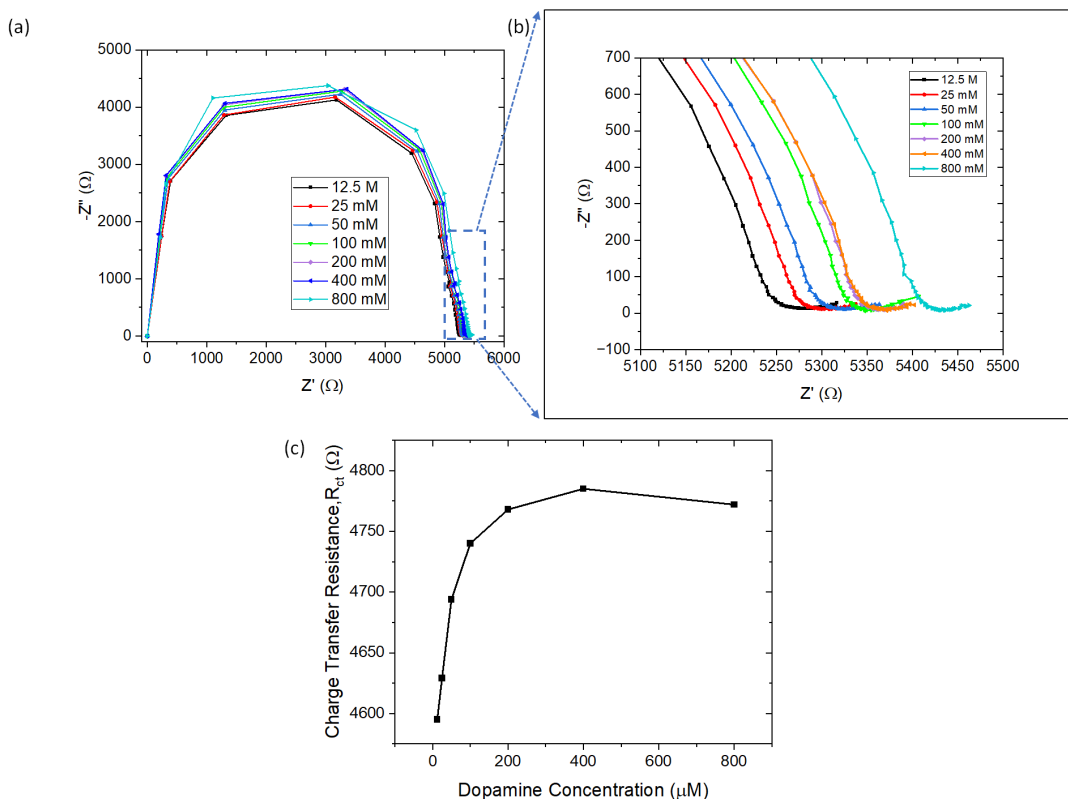


Figure 14: Double layer dip-coated paper-based biosensor (a) EIS characterization of dopamine detection from 12.5 μM to 800 μM , (b) enlarged view of (a), (c) Charge Transfer Resistance plot with dopamine concentration.

Table 1: Comparison of dopamine detection performance for different electrochemical biosensors based on conductive polymers.

Electrode Structure	Technique	Linear Range	Limit of Detection (LOD)	References
Polyaniline (PANI)–Au nanoparticles (NPs)	Differential pulse voltammetry (DPV)	10–1700 μM	5 μM	(Yang et al., 2012)
Polyaniline (PANI)–Au NPs	Linear sweep voltammetry (LSV)	20–100 μM	16 μM	(Mahalakshmi & Sridevi, 2021)
PEDOT:PSS (FET)	CV, DPV	5–100 μM	6 μM	(Gualandi et al., 2016)
PEDOT: PSS/Chitosan/Graphene	CV, DPV	0.05–70 μM	0.29 μM	(Shen et al., 2020)
MWCNT-PEDOT	CV, DPV	10–330 μM	10 μM	(Lin et al., 2010)
G-PEDOT:PSS	EIS	12.5–400 μM	3.4 μM	This work

TNF- α Detection. Similar to dopamine detection, EIS was performed to quantify the TNF- α using a Nyquist plot. The G-PEDOT:PSS electrode surface was first modified using UV-Ozone treatment, and the Nyquist plot before and after the UV-Ozone treatment was taken. It indicates that the surface underwent modification after UV-ozone as the resistance value increased. Figure 15a refers to the Nyquist plot for TNF- α concentration from 5 pg/mL to 50 ng/mL. R_{ct} with logarithmic x-axis (concentration) plot is presented in Figure 15b. The plot shows an almost linear straight line with a slope of 66.89. The limit of detection for TNF- α was ~ 5.97 pg/mL using the formula, $\text{LOD} = \frac{\sigma}{S}$ (σ is the standard deviation of the response and S is the slope = $0.13 \times (\text{slope of semi-log plot})$). Researchers adopted different structures and techniques for TNF- α detection. Poly(guanine)-functionalized silica NPs biosensor showed a detection range of 0.1–100 ng/mL and LOD of 50 pg/mL (Wang et al., 2006). Yin *et al.* developed an

alkaline phosphatase functionalized nanospheres based biosensors for TNF- α detection (range: .02–200.00 ng/mL, LOD: .01 ng/mL) (Yin et al., 2011). Au working electrode (range: 10–100 ng/mL, LOD: 10 ng/mL) (Liu et al., 2013) and comb structured gold microelectrode arrays (range: .001-1 ng/mL, LOD: 1 pg/mL) (Kongsuphol et al., 2014) based biosensors were also employed for TNF- α detection. Thus, our sensor shows similar high sensitivity as the gold electrode, which may require complicated processing and high cost. The performance comparison of different electrochemical biosensors mentioned above for TNF- α detection is tabulated in Table 2.

Table 2: Comparison of TNF- α detection of some electrochemical biosensors using different techniques.

Biosensor Structure	Sensing Matrix	Technique	Detection range	LOD	References
Poly(guanine)-Functionalized Silica NPs	Antibody	Square wave voltammograms	0.1–100 ng/mL	50 pg/mL	(Wang et al., 2006)
alkaline phosphatase functionalized nanospheres	Antibody	EIS	.02–200.00 ng/mL	.01 ng/mL	(Yin et al., 2011)
Au working Electrode	Aptamer	CV	10–100 ng/mL	10 ng/mL	(Liu et al., 2013)
Comb structured gold microelectrode arrays	Antibody	EIS	.001-1 ng/mL	1 pg/mL	(Kongsuphol et al., 2014)
G-PEDOT:PSS	Antibody	EIS	.005-50 ng/mL	5.97 pg/mL	This work

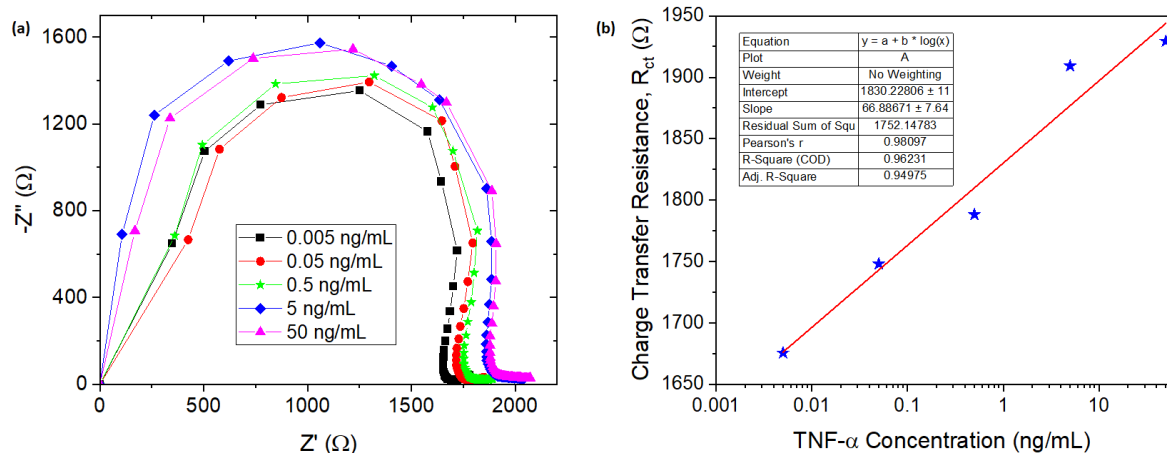


Figure 15: Paper-based biosensor (a) EIS characterization of TNF- α detection from 0.005 ng/mL to 50 ng/mL, (b) Charge transfer resistance plot with the logarithmic scale of TNF- α concentration (red straight line depicts calibration curve).

IL-6 Detection. For IL-6 detection in a wide range (0.002-2000 ng/mL), EIS was performed in a similar fashion to TNF- α . Figure 16a-b shows the Nyquist plot for IL-6 detection. Charge transfer resistance (R_{ct}) increases with IL-6 concentration (Figure 16c). Similar to dopamine and TNF- α detection, the limit of detection of our paper-based biosensor was calculated using the formula, $LOD = \frac{3.3\sigma}{S}$, and LOD was ~ 9.55 pg/mL. Previously, Russel *et al.* developed an Au based needle shaped microelectrode for IL-6 detection (range: 20-100 pg/mL, LOD: 20 pg/mL) (Russell et al., 2019). Graphene oxide (GO) based liquid-gated FET biosensors were also used to detect IL-6 in a range of 4.7-300 pg/mL (LOD: 1.53 pg/mL) (Huang et al., 2015). In comparison to our paper-based biosensor, the above-mentioned microelectrode/FET needs complex and costly manufacturing process to get almost similar sensitivity.

Selective Detection of IL-6. With the specific antibody attached to the biosensor, the specific antigen can bind with the antibody. Otherwise, using a different antigen will not change the R_{ct} . Using this principle, IL-6 was first detected in paper-based biosensors. Then, 2 μ L of

Serpin A1 antigen was poured into the existing solution to check the EIS performance. Firstly, PBS and IL-6 were added, and there was a significant shift from PBS run to IL-6 due to antigen attachment. However, there was no significant charge transfer resistance change after Serpin A1 addition which means no Serpin A1 attachment with the IL-6 antibody (Figure 16d). Adding up to 6 μL of Serpin A1 antigen, no resistance change was observed compared to IL-6 and thus signifies that our paper-based is highly selective.

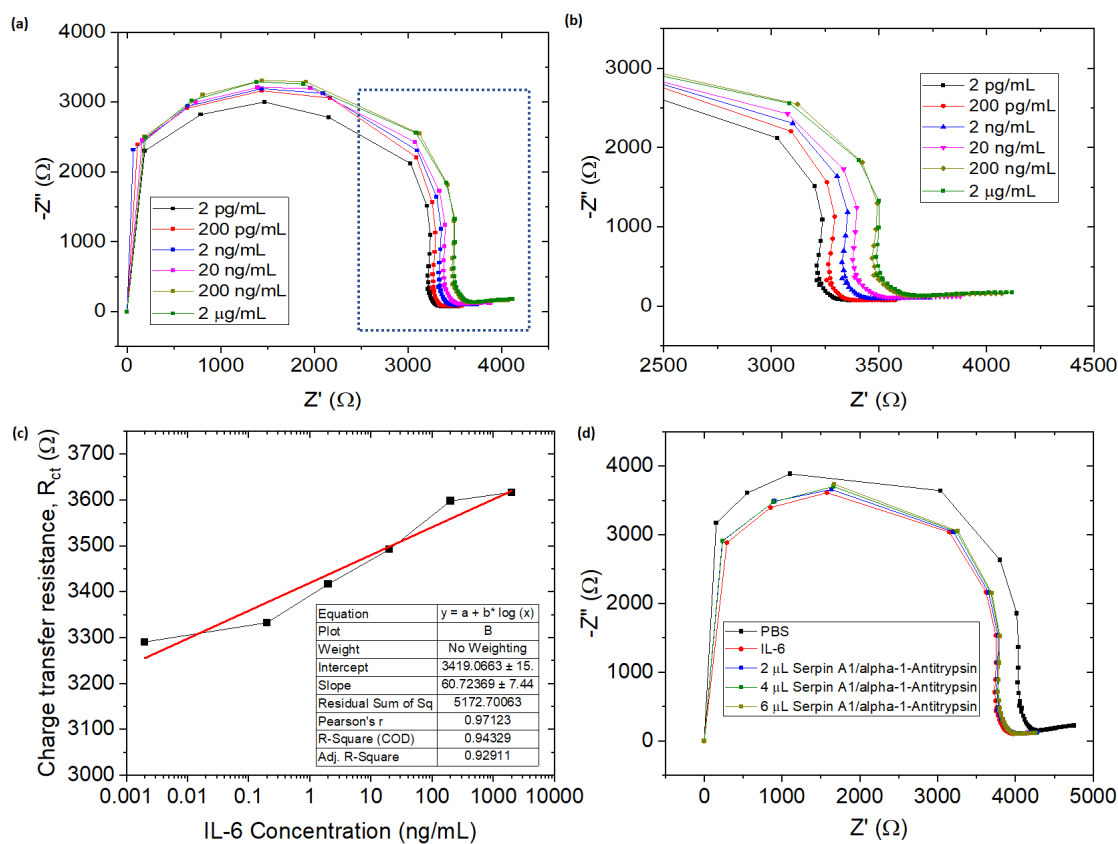


Figure 16: Paper-based biosensors' (a) EIS characterization of IL-6 detection from 0.002 ng/mL to 2000 ng/mL, (b) enlarged view of (a), (c) Charge transfer resistance plot with the logarithmic scale of IL-6 concentration (red straight line depicts calibration curve), (d) Selective detection of IL-6.

CHAPTER III

2D NANOMATERIAL BASED ENERGY GENERATION/STORAGE DEVICES

Nanogeneration Using Nanofiber Composite

Nanogeneration Using Water Waves

The same nanofiber mentioned in Chapter II, Section: Nanofiber Based Sensing was used for the test. Using an Arduino-controlled peristaltic pump, different flow rates with different amplitudes of artificial water waves were created. The corresponding flow rates for different Arduino signal on and off timing are listed in Table 3.

Table 3: Peristaltic Pump characteristic flow rate with control time.

Case	Signal On time (ms)	Signal Off time (ms)	Flow Rate (ml/min)
1	1000	100	30
2	1000	500	24

These artificial waves were created to examine the performance of the PVDF/PAni sample nanogeneration with and without graphene incorporation. The sample G@PVDF/PAni generates higher peak-to-peak voltages than the PVDF/PAni. The maximum voltage generation in G@PVDF/PAni is 40.6 mV peak to peak (pk to pk), whereas for the PVDF/PAni it's only 11.2 mV pk to pk (Figure 17a-b). Similarly, for the second case, the maximum voltage generation for G@PVDF/PAni is 43.2 mV while the PVDF sample is producing 28.4 mV

(Figure 17c-d). The voltage generation was due to the bending of the sample which causes the surface charges to release. As the waves were approaching with different forces (due to signal pulses provided by Arduino) towards the PVDF/PAni, voltage generation was changing over time. This can be very useful to utilize the tidal wave energy using this kind of piezoelectric material.

Table 4: Performance of different nanocomposite nanogenerators based on PVDF.

Fillers	Fabrication	Test Method	Max. Voltage Output	Max. Current Output	References
Graphene (1.6 %)	Electrospinning	3 Point Bending (1 mm displacement)	0.5 V	-	(Abbasipour et al., 2019)
Graphene (0.1 %)	Electrospinning	Finger Tap-in	7.8 V	4.5 μ A	(Abolhasani et al., 2017)
-	Electrospinning	5 g Weight Dropping	0.028 V	-	(Gheibi et al., 2014)
Graphene Oxide (0.4 %)	Electrospinning	Finger tap-in	1.5 V	-	(Zeyrek Ongun et al., 2020)
PAni & HNT (halloysite nanotube)	Electrospinning	Impact loading (14g weight from 10 cm height)	7.20 V	0.75 μ A	(Khalifa et al., 2019)
Graphene & PAni	Forcespinning	Finger Tap-in	0.075 V	24 mA	This work

Vibration Analysis

Vibration is a common phenomenon of back-and-forth motion in opposite directions to an axis. A mini vibrating motor was used to create the fluctuating vibrating motion, and the motor was attached to the PVDF/PAni and G@PVDF/PAni nanofibers (Figure 18a). BK Precision Triple Output Programmable DC Power Supply (Model 9130B) was used to supply the power for the motor (2V-4V). As the voltages increased, the vibration of the motor increased. By recording the sound via a smartphone and analyzing the frequency using Audacity software, vibration magnitude was qualitatively determined from the sound level. The motor vibration increased with increasing motor operating voltages for a fixed frequency range (Figure 18b). Vibration motor sound characteristic means vibration magnitude in dB (for 2V supply) and corresponding sample voltage generation for 0.1 seconds is also shown in Figure 18c. The induced voltages follow a pattern related to motor-generated vibration.

The root means square voltage (V_{RMS}) generated by the sample increased with the motor vibration magnitude level for the PVDF/PAni nanofiber (Figure 18d). Similarly, with the G@PVDF/PAni nanofiber, the voltage generation increased around 2 times that of the PVDF/PAni nanofiber at similar motor vibration. Comparing the piezoelectric performance of different filler-based PVDF nanogenerators is given in Table 4. The maximum voltage and current of our sample using simple finger tap-in was around 0.075 mV and 24 mA, hence having a better electrically conductive network as the current amount is significantly higher (in the mA range) than reported by others (mostly in μA , nA range).

Graphene added by the drop-casting method increases the conductivity of the PVDF/PAni network, hence we got 5 times better sensitivity in temperature sensing, ~ 4 times better voltage generation in normal finger tap-in, and ~ 3.6 times higher voltage generation in nanogenerator using water wave than the normal PVDF/PAni fiber mats (Table 5).

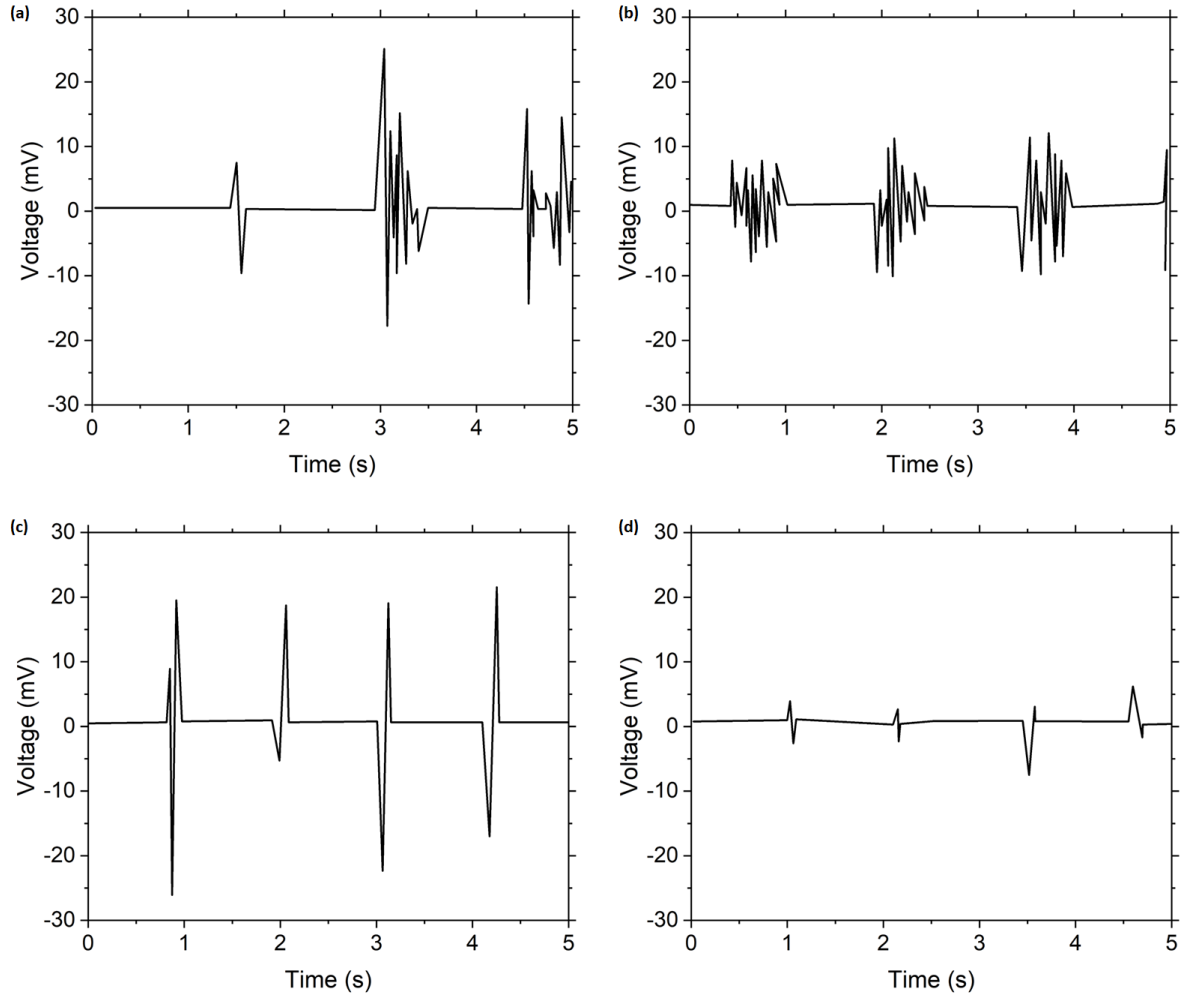


Figure 17: Voltage signal for pump switch on 1000 ms and switch off 100 ms of (a) G@PVDF/PAni PENG, (b) PVDF/PAni PENG. Voltage signal for pump switch on 1000 ms and switch off 500 ms of the (c) G@PVDF/PAni PENG, (d) PVDF/PAni PENG.

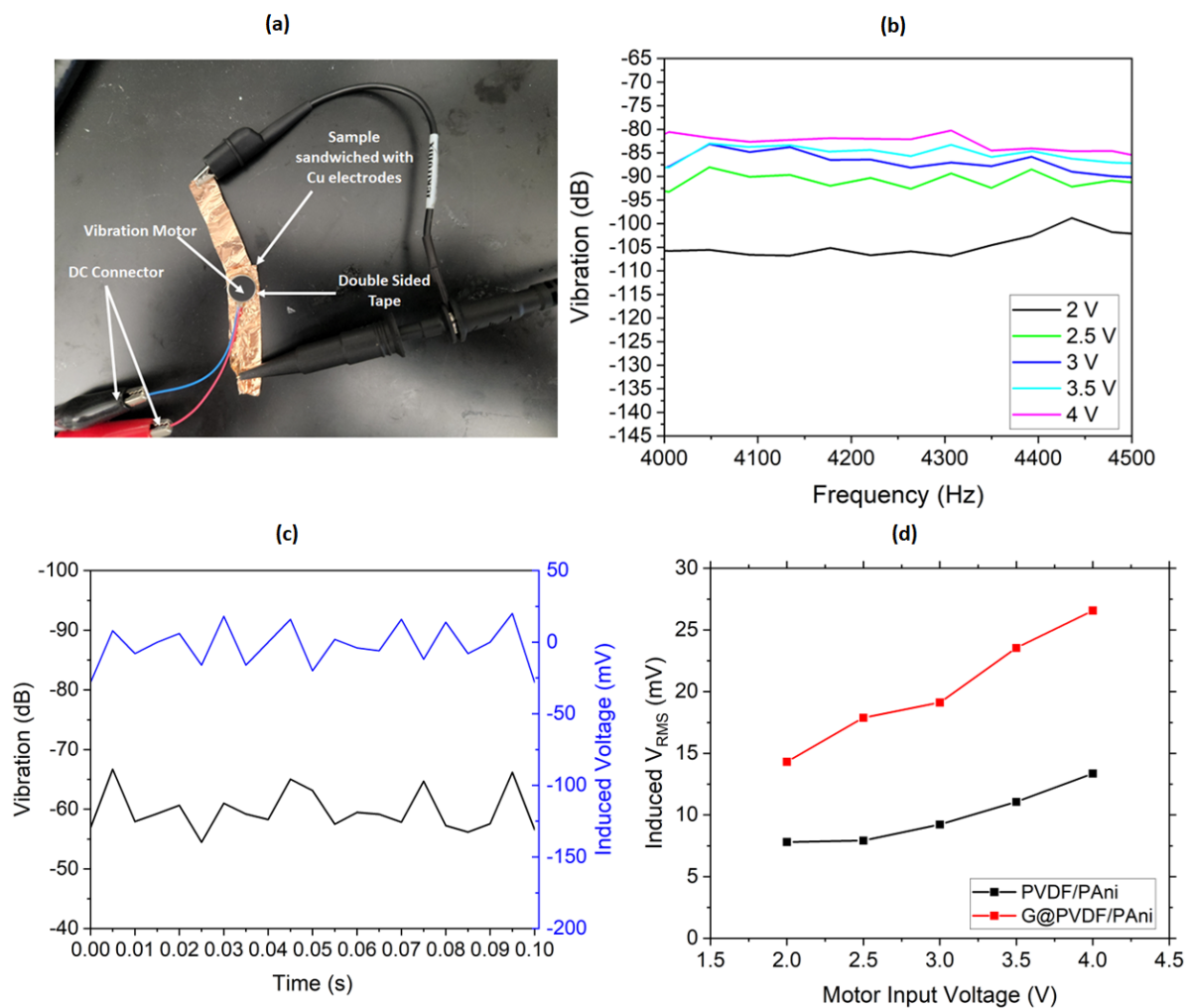


Figure 18: (a) Setup image of sample and vibration motor, (b) Vibration (dB) vs Frequency (Hz) plot for different voltages, (c) Vibration motor sound characteristics (for 2V DC supply) and corresponding sample voltage generation for 0.1 seconds, (d) Sample induced V_{RMS} Vs. vibration motor operating voltage.

Table 5: Performance differences between PVDF/PAni and G@PVDF/PANI for all sensing and nanogeneration applications.

	Parameters	PVDF/PAni	G@PVDF/PANI	Percentage Difference
Temperature Sensing	Resistance change at 50 (°C)	5 (%)	25 (%)	~ 400 (%)
Finger Tap-in	Max. Voltage generation (pk-to-pk)	18 mV	75 mV	~317 (%)
	Max. Current (pk-to-pk)	14 mA	24 mA	~ 71 (%)
Nanogeneration Using Water Waves (pump switch on 1000 ms and off 100 ms)	Max. Voltage generation (pk-to-pk)	11 mV	40 mV	~ 264 (%)
Nanogeneration Using Water Waves (pump switch on 1000 ms and off 500 ms)	Max. Voltage generation (pk-to-pk)	43 mV	28 mV	~ 54 (%)
Vibration Analysis	Voltage Generation at vibration motor input voltage 4 V	26 mV	12.5 mV	~ 108 (%)

CVD Coated Nanofiber Anode for Enhanced Battery Performance

Because of the growing population, the reliance on fossil fuels for energy generation and storage has had a substantial impact on the climate. Researchers have put significant effort into exploring new materials and designing novel structures for high-energy-density LIBs as energy storage (reference). Graphite which is the most popular commercial anode material for LIBs due to its low cost, and low flat working potential. However, the theoretical capacity for graphite is only 372 mAh/g which is not sufficient to meet the high energy-storage demands. Significant attention has been focused on researching new anode materials with higher capacities to replace the graphite anode structure in LIBs. In this study, chemical vapor deposition (CVD)-synthesized pyrolytic carbon coating on SnO₂/TiO₂ short fibers demonstrated as a high-performance anode material in lithium-ion batteries due to its high electrical conductivity, high surface area, and good stability during charge/discharge cycling.

CVD Carbon Coatings

SnO₂/TiO₂ (3:1) short fibers were fabricated using Forcespinning method. Short fibers of SnO₂/TiO₂ (3:1) were put in a quartz boat and coated with carbon in a tube furnace (schematic is shown in Figure 19. Schematic of Chemical Vapor Deposition Setup. With argon flowing through the chamber at a rate of 160 standard cubic centimeters per minute (SCCM), the material was heated to 1000°C at a rate of 33°C/min. 32 SCCM of methane (CH₄) gas was introduced into the furnace after it reached 1000°C to allow for the carbon coating process. To examine the effects of CVD on the electrochemical performance of SnO₂/TiO₂, two different coating times - 30 minutes and 60 minutes - were used. The recipe for the CVD process is shown in Figure 20. After coating, the furnace was allowed to cool to room temperature before the material was

removed. The material was crushed to a fine powder using a Hauschild Speed Mixer (DAC 150.1 FVZ-K) at 2300 rpm for 5 minutes with 2 mm Zirconia ceramic beads.

Characterization

Raman spectra were recorded by an NRS-4500 Confocal Raman spectrometer (Jasco) with a 100× objective lens (NA = 0.9) and a 900 grooves/mm grating. Green (532 nm) laser was used as the excitation source while keeping the laser power at 0.7mW to avoid laser-induced heating. Slit of $50 \times 8000 \mu\text{m}$, exposure time of 20 sec, and 3 accumulations were selected to optimize the peak-to-noise ratio and reduce fluorescence. Multiple points on various particles from each sample were measured on a silicon wafer to increase the confidence in results.

Carbon coating thickness, crystal structure, and uniformity on the nanofiber surface were analyzed using JEOL JEM-1230 Transmission Electron Microscope after dissolving the nanofibers in solvent and drop casting on carbon-coated Cu TEM grid.

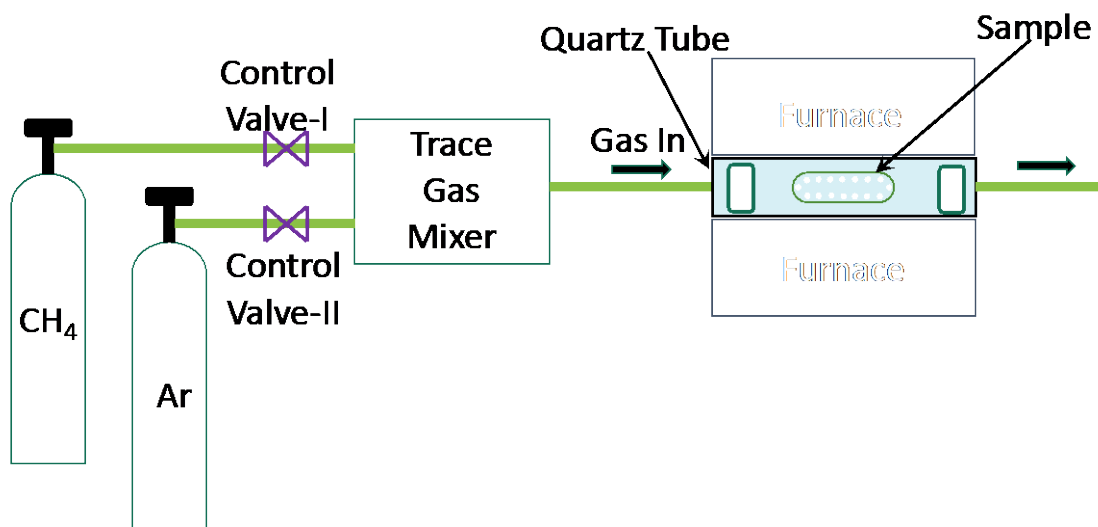


Figure 19: Schematic of Chemical Vapor Deposition Setup.

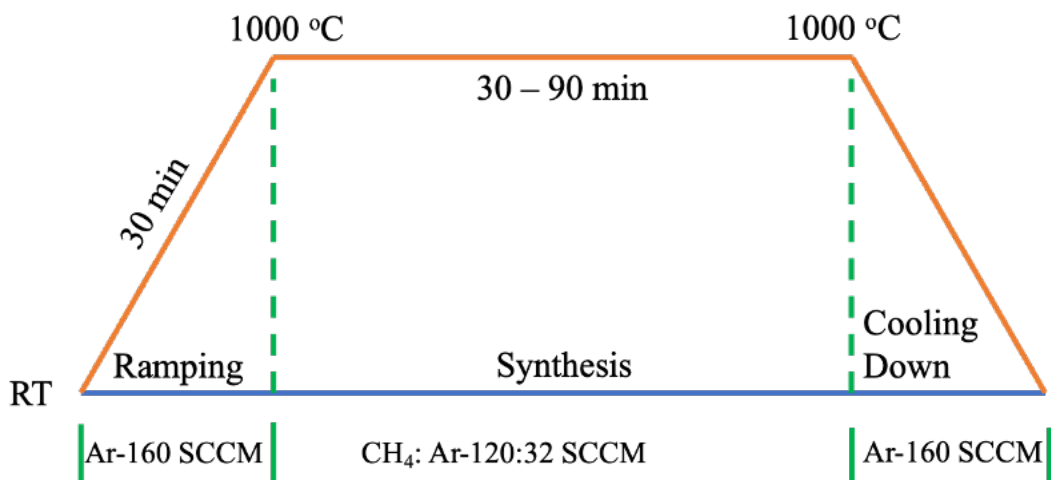


Figure 20: Recipe for pyrolytic carbon coating on SnO₂/ TiO₂ short fibers.

Raman and TEM. Raman spectroscopy was carried out on the CVD-coated samples. The carbon coating on the SnO₂/TiO₂ short fibers has distinct peaks at $\sim 1360 \text{ cm}^{-1}$ (D band) and 1580 cm^{-1} (G band) along with a 2D band $\sim 2690 \text{ cm}^{-1}$ (Figure 21a). The abovementioned peaks depict the pyrolytic carbon (Similar to graphite, where graphene layers are stacked in parallel, pyrolytic carbon additionally includes translation and/or rotation about the graphene plane) coating on the short nanofibers. G bands correspond to the in-plane vibration of carbon atoms, and the D band represents the defect-induced double resonant scattering (López-Honorato et al., 2010; Thomsen & Reich, 2000). The weak second-order 2D bands refer to the three-dimensional ordering (in c-direction) of pyrolytic carbon. Intensity ratio of the D band to the G band (I_D/I_G) of smaller than unity indicates a good crystallinity, which means a better graphitization degree and more stable carbon coating.

Transmission electron microscopy images at different magnifications were also taken to further study the structure and morphology of the SnO₂/TiO₂ coated fibers. Figure 21b-e shows the pyrolytic carbon coating dimension of $\sim 9.25 \text{ nm}$ on the short nanofibers. By analyzing different images, the coating dimension at different spatial locations was in the range 6-10 nm.

Also, the coating enables a much more stable layer that protects the short, composite fibers. The amorphous pyrolytic carbon coating can also be verified from the distinct d-spacing (3.2 Å). The Selected area electron diffraction (SAED) showed the polycrystallinity of the pyrolytic carbon as concentric circles with different diameters. Therefore, the CVD pyrolytic carbon coating acted as a protective surface which improved the cycle performance of the anodes.

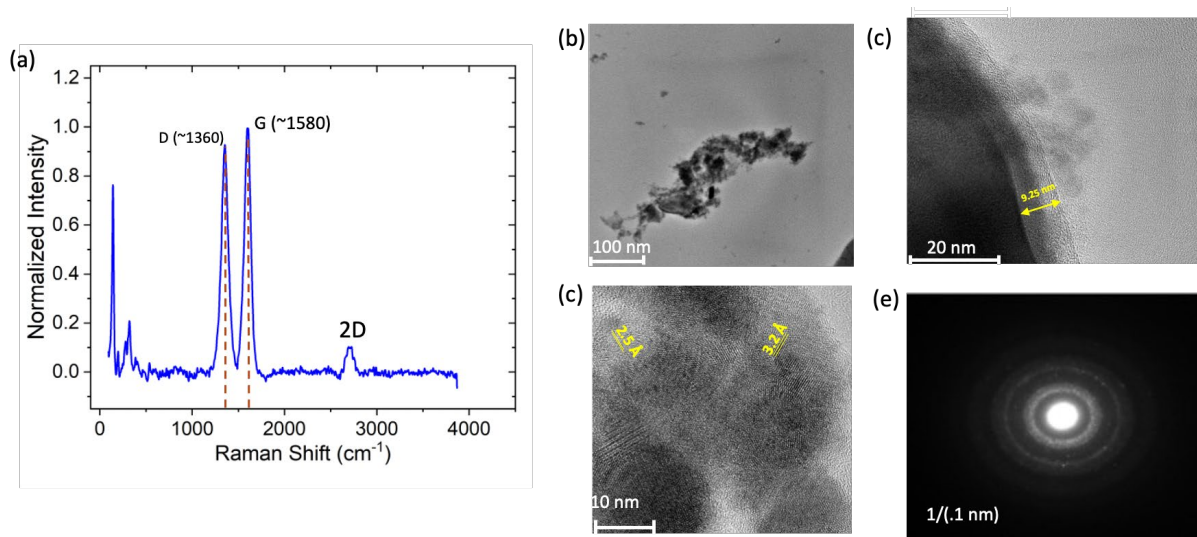


Figure 21: (a) Raman spectroscopy of pyrolytic carbon coated short nanofibers sample, (b-e) TEM images of pyrolytic carbon (polycrystalline) coated SnO₂/TiO₂ short fibers.

Performance of non-coated vs CVD coated Sample. The specific capacity of the coated (30 min and 60 min samples) and non-coated (0 min) with the cycle is shown in Figure 22. Non-coated short fiber specific capacity decreases more rapidly than CVD coated sample. The 60 min CVD coated sample showed an initial capacity of 450 mAh g⁻¹, However, it started increasing after 38 cycles and the capacity surpasses the non-coated sample specific capacity at that cycle. On the other hand, the 30 min coating showed higher initial capacity than 60 min, and it continues to maintain the capacity at that constant value.

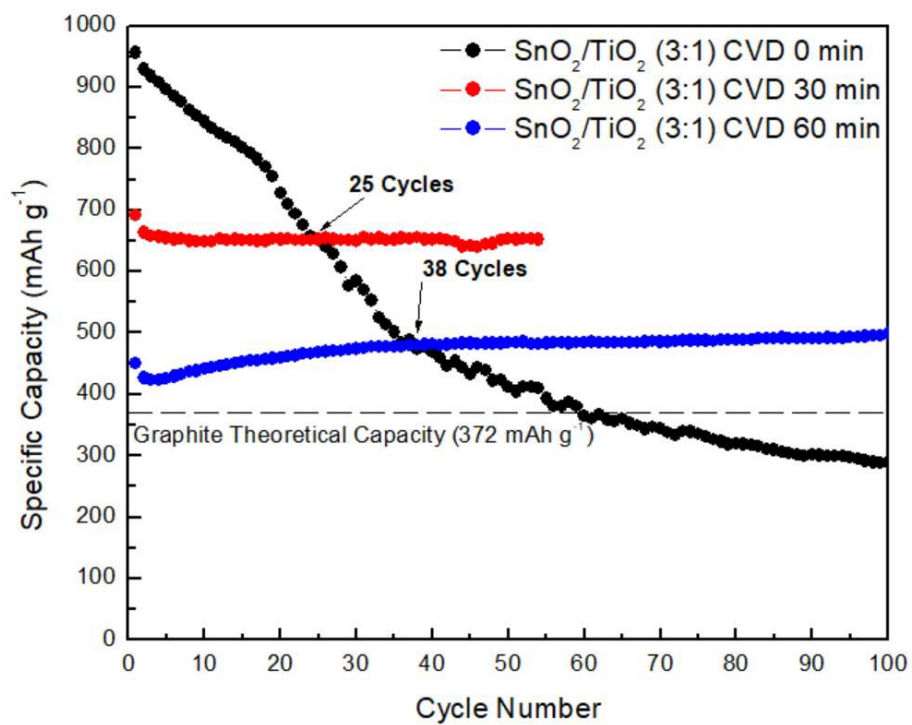


Figure 22: Performance Analysis of CVD-coated SnO₂/ TiO₂ short fibers (acknowledgment: performed by David Sanchez).

CHAPTER IV

NANOCOMPOSITE INK BASED SEPARATION DEVICES

Direct Ink Writing of Polymer Nanocomposite Membrane

3D printing or additive manufacturing has become an attractive field as it has the advantages like fabrication of customized complex shapes with high resolution within a significantly short time. Compared to traditional manufacturing processes, additive manufacturing reduced material consumption and wastage. Additive manufacturing has become a beneficial manufacturing process for the last few decades for industries like aerospace, automotive, biomedical, electronic, and sensor fabrication industry. Among all the 3D printing technologies available, fused deposition method (FDM), stereolithography (SLA), selective laser melting (SLM), selective laser sintering (SLS), and direct ink writing (DIW) are most common. Each of the technologies has certain advantages and disadvantages. However, direct ink writing (DIW) provides the flexibility to select a variety of customized ink for different applications. Additionally, the process is inexpensive, easy, and adaptable to use. It is an extrusion-based printing system where non-Newtonian inks are used with appropriate rheological properties.

Fabrication of Ink

Ecoflex 0030-part A and part B with 20% of graphite (obtained from Asbury carbon, lateral size $\sim 850 \mu\text{m}$) was taken in a container and mixed in Hauschild speed mixer at 2500 rpm for 6 minutes with the help of 12.7 mm cylindrical ceramic beads. Then the ink was screened through a 40x40 nichrome wire mesh to filter out the larger graphite flake.

Printing Parameters Optimization

Both part A and part B were mixed and taken into EMO header (Hyrel 3D, USA). The nozzle used for printing on the metal mesh was taper luer lock type (gauge 20). As the ink used in printing was shear thinning in nature, appropriate filler content is necessary for maintaining its shape after the printing on 20x20 stainless steel metal mesh (wire dia. $\sim 460\text{ }\mu\text{m}$ and gap between wires $\sim 810\text{ }\mu\text{m}$). As the elastomeric composite gets expanded after the printing, an optimal printing width with a specified gap is needed to create pores in the metal mesh wire. The elastomeric high viscous composite ink is semi-solid in nature, however, due to high shear forces generated by the header screw, the shear thinning behavior was observed. Both horizontal lines and vertical lines were printed using a Hyrel Engine HR printer to mimic printing exactly on the metal mesh wires (the schematic is shown in Figure 23). The lines got cured immediately after the printing due to bed heating as the temperature accelerates the curing kinetics. For a specific line printing, optimization of layer height (distance between luer dispensing tip and metal mesh substrate), layer width and height, printing speed (traveling speed of bed in mm/s), material flow rate (which depends on layer width, layer height, extrusion multiplier, printing speed). For The optimized parameter is shown in Table 6.

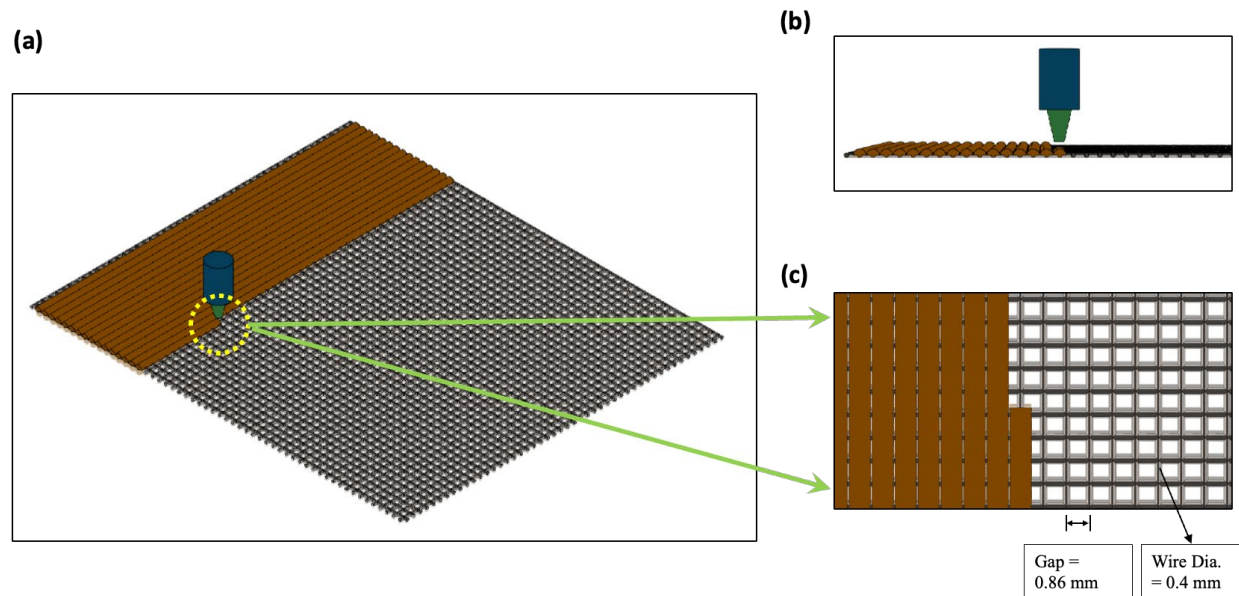


Figure 23: (a) Schematic of high viscous Direct ink writing printing on metal mesh, (b) Front view of (a), (c) enlarged view of (a).

Table 6: Optimized parameters for printing on a 20x20 Stainless Steel Metal Mesh as a Membrane for water desalination.

Parameters	Value
Nozzle Dia.	Gauge 20 (~600 μm)
Bed Temperature	60 $^{\circ}\text{C}$
Height	2 mm
Printing Speed	10 mm/s
Extrusion Multiplier	1
Layer Width	600 μm
Layer Height	1 mm
Gap between adjacent lines	100 μm

Testing of 3D Printed Membrane

Fabrication and Characterization

Fabrication. The printing on the stainless-steel metal mesh was used as a membrane for water desalination applications. As for membrane distillation (MD), the membrane should have hydrophobic characteristics. So, the water contact angle was performed using a goniometer and image processing software. In membrane distillation, two water streams (feed side which is salty, permeate side which is freshwater) are separated by a hydrophilic membrane. As the salt water is heated, it produces water vapor which creates a partial water vapor. The smaller pores only permit the water vapor to go through the membrane. The only driving force here is the partial vapor pressure generated due to the thermal gradient between the two streams. the salty water remains back in the feed stream. As a result, the freshwater quantity increases with time. The detailed schematic of the membrane distillation process is also shown in Figure 24.

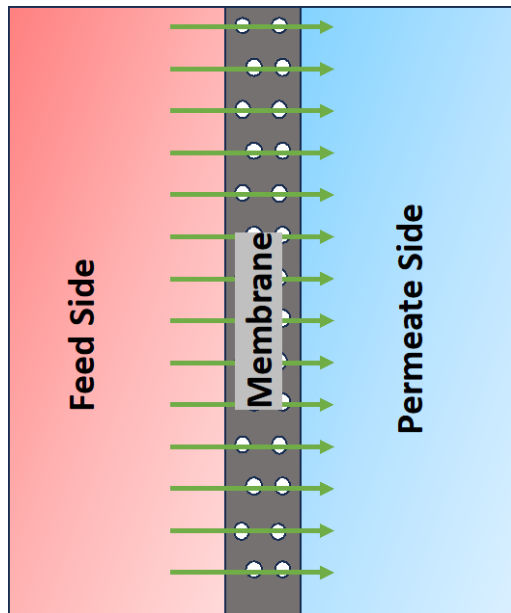


Figure 24: Schematic of membrane distillation process.

Characterization (Water Contact Angle). Printing on the metal mesh membrane with the 20% G Elastomer ink was done on one side and double side on the metal mesh to impact the water contact angle. Figure 25a shows the water contact angle measurement at different spatial locations. For one side printing, the water contact angle varied from 93° to 101° whereas the water contact angle for both side printing was 95° – 102° (Figure 25b).

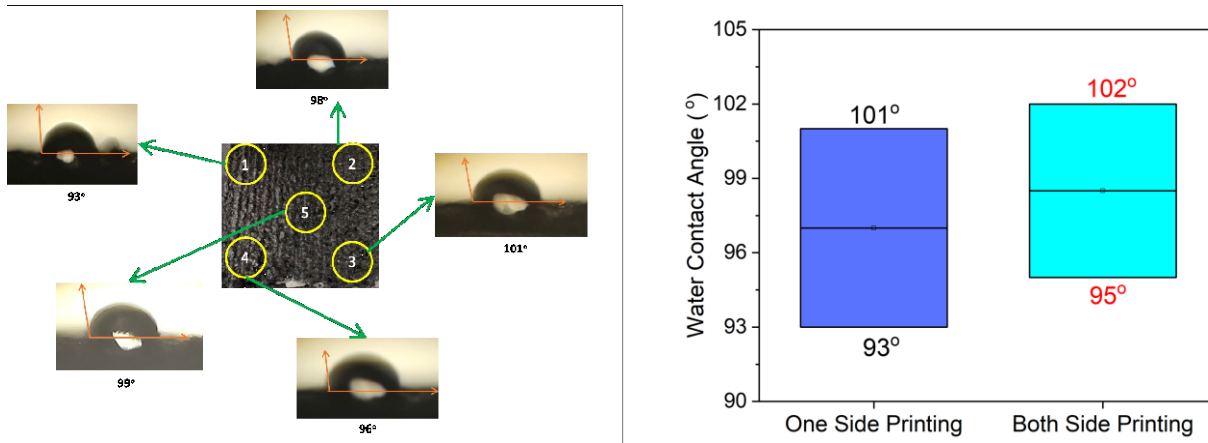


Figure 25: (a) Water contact angle at different locations of the membrane, (b) comparison of the water contact angle for one side printing and both side printing membrane.

Setup for Membrane Distillation. Two pumps were used to run the feed side (salt water) and permeate side (freshwater) fluid circuit. A hot plate and a jacket heater were used to heat the feed side water uniformly in a beaker. A DC programmable triple output power source was used to run the 12 V DC pump. Additionally, a weighing scale and a total dissolved solids (TDS) meter were used to measure the live weight of the permeate side and TDS in ppm respectively. The membrane holder (two parts: top and bottom shown in Figure 26a-b) was designed using Inventor software. The setup for the MD test used in this study is shown in Figure 26c.

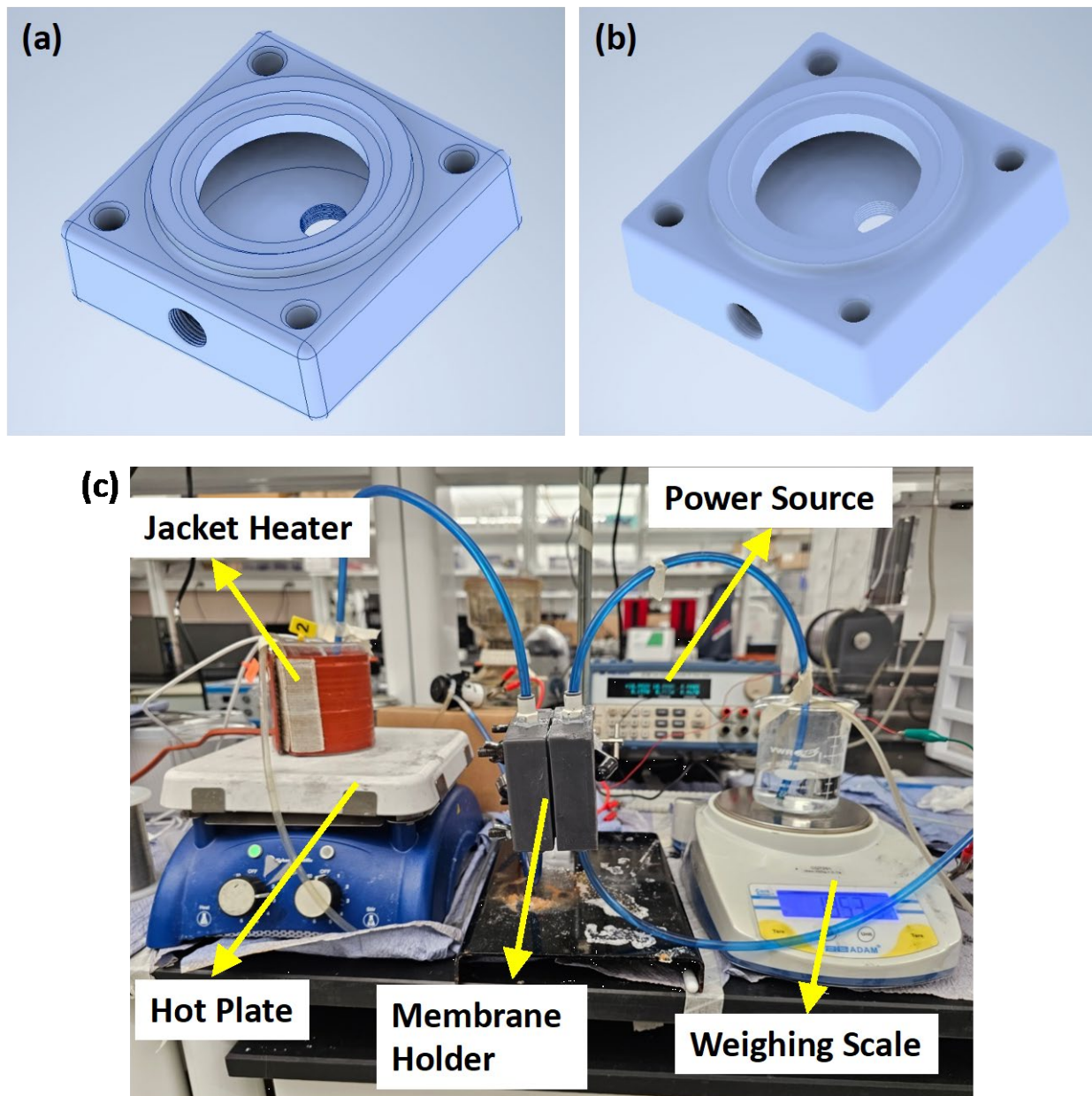


Figure 26: CAD drawing of the membrane holder (a) top part, (b) bottom part. (c) Setup for membrane distillation using DIW printed metal mesh membrane.

Performance of DIW printed Metal Mesh Membrane

DIW Printed Membrane with Metal Wire Treatment. The fabricated membrane using direct ink writing was highly dense, so metal wire brush was used to make holes in the elastomeric composite ink membrane. As elastomer comes back to its original shape after removing the force, the effective hole was small enough for the required pore size of membrane distillation applications. This membrane was then deployed with a feed stream salt ppm level of 3485, and the ppm level and water level were measured from 2-5 hours (data taken every hour) after turning on both pumps. Figure 27 shows that the initial flux obtained after 2 hours of operation was close to $1.35 \text{ L m}^{-2} \text{ hr}^{-1}$ (effective dia. of membrane = 40 mm) and it increases up to 2.6 at 4 hours. However, the flux started decreasing after that, and the flux was $1.8 \text{ L m}^{-2} \text{ hr}^{-1}$ after 5 hours of operation. As the freshwater ppm level is <1000 , we operated the system for 5 hours (ppm – 841). On the other hand, the rejection rate was initially $\sim 94\%$, and it then started decreasing (reached 75% after 5 hours of operation).

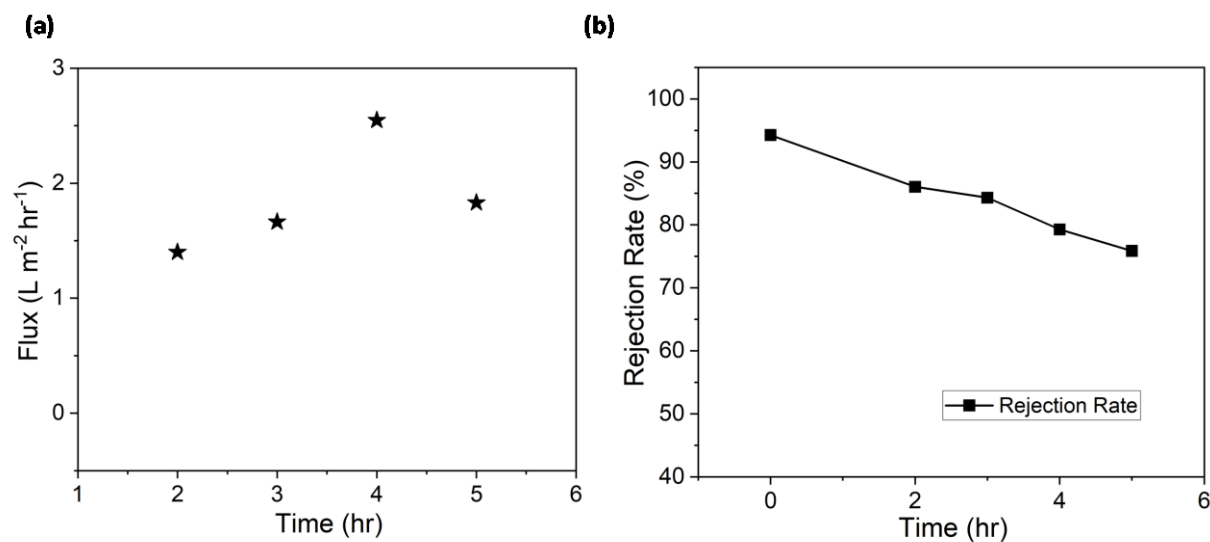


Figure 27: Performance of the metal mesh membrane. (a) flux and (b) rejection rate plot with hours of operation.

DIW Printed Membrane with Laser Treatment and Electrical Current

The metal mesh membrane flux was low after 5 hours of operation, so the membrane was laser treated to create control pores for vapor passing through the membrane. The parameters for the laser treatment (speed, power, dots per inch, focusing) were optimized. A specific CAD was designed, and holes were created every 1 mm apart. Two Al wires were attached to the laser-treated membrane to create an electric field as the membrane and metal mesh both were conductive in nature. The effect of laser treatment and electrical current can be understood from the water flux and rejection rate performance of the membrane (Figure 28). The flux was $\sim 12 \text{ L m}^{-2} \text{ hr}^{-1}$ after 15 minutes of operation, then it started decreasing. However, it reached $4.5 \text{ L m}^{-2} \text{ hr}^{-1}$ of flux after 90 minutes of operation (ppm level was 989) as the pores are more open than the previous one. The rejection rate of the salt was 98% initially, and it reached to 85% after 90 min. The rejection rate and the flux performance were much better than the previous membrane. It can be inferred that the laser treatment of the membrane increases the porosity (thus increasing the flux), and the electrical current flowing (electrical field) through the membrane helps in much better salt rejection.

The total amount of flux after 90 min. of operation was 11 g, and to check whether the system was performing the actual membrane distillation or it was just a leak, we performed a control test. We took the exact amount of fresh water with ppm 116 that we started our experiment on fresh permeate side. Then we mixed 11 g of feed water of ppm 6595 with the fresh water, and the ppm level of the mixture was 1316. From our experiment, we got the last ppm level of 989. So, it can be verified from the membrane rejects around 25% salt during the desalination process.

Again, this membrane is further tested with a high saline feed stream (ppm level of 35000). The membrane worked for up to 30 minutes with a total amount of flux obtained was 1.7g within 30 minutes. As the salinity of the feed stream was much higher, the pores may get clogged after 30 minutes. Thus, this 3D-printed membrane can be an amazing alternative for harvesting fresh water from both low and high-saline sources.

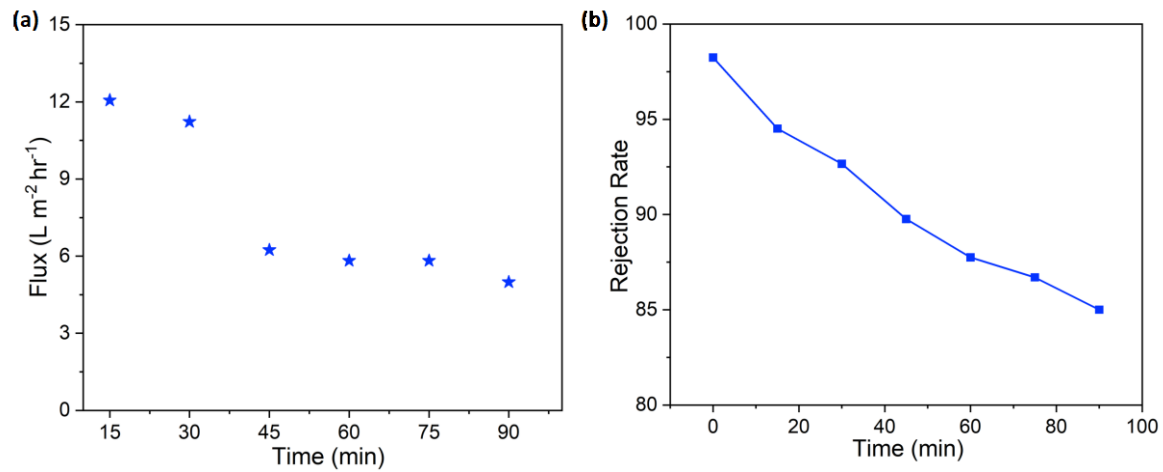


Figure 28: Performance of the laser treated and electrical current applied metal mesh membrane.

(a) flux and (b) rejection rate plot with hours of operation.

CHAPTER V

CONCLUSION

Conductive PVDF/PAni nanofiber mats were prepared using the forcespinning method. Mats were coated with a graphene solution using a drop-casting process. The conductivity of coated nanofiber mats was increased, and promising results for the application in temperature, touch, and airflow sensing were reported. The open-circuit voltage generation of the graphene-coated sample using acetone was about 3 times higher than the sample prepared using IPA. G@PVDF/PAni and PVDF/PAni were then investigated to harvest the water tidal energy and vibration energy. It was concluded that the G@PVDF/PAni-based nanogenerator induced 3.6 times and 2 times higher voltages than PVDF/PAni in tidal energy and vibrating energy harvesting methods, respectively. The obtained results pave the way for the potential application of the developed PVDF/PAni nanofiber-based mats as temperature and airflow sensing as well as water tidal energy harvesting nanogenerators.

Paper-based biosensors have shown a lot of promise in recent years due to their simplicity, high sensitivity, ease of use, portability, accessibility, and low cost. Furthermore, these sensors can provide data quickly without the need for a laboratory or a skilled individual. In this study, a paper-based electrochemical sensor with G-PEDOT:PSS (graphene and conductive polymer) has been developed, and it demonstrated excellent performance in detecting dopamine, TNF- α , and IL-6 using electrochemical impedance spectroscopy. The detection range for dopamine, TNF- α , and IL-6 was 12.5-400 μ M, 0.005-50 ng/mL, 0.002-2000 ng/mL

respectively. Additionally, the detection limit was 3.4 μM , 5.97 pg/mL , and 9.55 pg/mL exemplifying that our paper-based biosensor can be a promising avenue for early cancer detection, chronic wound monitoring, or immune sensing. Thus, these paper-based sensors offer an alternate, excellent, and reliable platform for immune sensing or early diagnosis even in countries with limited resources.

An elastomer sensor incorporating in situ graphene formation from graphite can detect different human motions such as finger bending, elbow bending, pulse, respiration, and voice recognition. Flexible keypads were also fabricated with these highly conductive sensors. By detecting the resonance frequency, a low-cost passive wireless sensor was also included, and it may be utilized to assess various physical activity signals for remote health monitoring. As a result, these multifunctional, low-cost G-EMC sensors can be used in a variety of applications that can be revolutionary to flexible electronics.

Pyrolytic carbon coating on short fibers via CVD outperformed the non-coated battery anodes in terms of specific capacity due to its inherent structure. Additionally, polymer composite ink prepared by high-shear planetary mixing was used for fabrication of direct ink writing membrane on metal mesh. The membrane was further treated with laser and an electrical current was applied to enhance both the flux and salt rejection rate. This study discussed the synthesis of 2D nanomaterial and nanocomposites using different approaches, and their application in various sensing, energy generation/storage devices, and membrane distillation.

REFERENCES

- Abbasipour, M., Khajavi, R., Yousefi, A. A., Yazdanshenas, M. E., Razaghian, F., & Akbarzadeh, A. (2019). Improving piezoelectric and pyroelectric properties of electrospun PVDF nanofibers using nanofillers for energy harvesting application. *Polymers for Advanced Technologies*, 30(2), 279-291.
- Abolhasani, M. M., Shirvanimoghaddam, K., & Naebe, M. (2017). PVDF/graphene composite nanofibers with enhanced piezoelectric performance for development of robust nanogenerators. *Composites Science and Technology*, 138, 49-56.
- Adabi, M., Esnaashari, S. S., & Adabi, M. (2021). An electrochemical immunosensor based on electrospun carbon nanofiber mat decorated with gold nanoparticles and carbon nanotubes for the detection of breast cancer. *Journal of Porous Materials*, 28, 415-421.
- Adkins, J., Boehle, K., & Henry, C. (2015). Electrochemical paper-based microfluidic devices. *Electrophoresis*, 36(16), 1811-1824.
- Akbari, M., & Hassan-Zadeh, V. (2018). IL-6 signalling pathways and the development of type 2 diabetes. *Inflammopharmacology*, 26(3), 685-698.
- Allothman, Z. A., Bukhari, N., Wabaidur, S. M., & Haider, S. (2010). Simultaneous electrochemical determination of dopamine and acetaminophen using multiwall carbon nanotubes modified glassy carbon electrode. *Sensors and Actuators B: Chemical*, 146(1), 314-320.
- Amjadi, M., Kyung, K.-U., Park, I., & Sitti, M. (2016). Stretchable, Skin-Mountable, and Wearable Strain Sensors and Their Potential Applications: A Review. 26(11), 1678-1698. <https://doi.org/10.1002/adfm.201504755>
- Amjadi, M., Yoon, Y. J., & Park, I. (2015). Ultra-stretchable and skin-mountable strain sensors using carbon nanotubes–Ecoflex nanocomposites. *Nanotechnology*, 26(37), 375501.
- Anik, Ü. (2017). Electrochemical medical biosensors for POC applications. In *Medical biosensors for point of care (POC) applications* (pp. 275-292). Elsevier.
- Anuar, N. S., Basirun, W. J., Shalauddin, M., & Akhter, S. (2020). A dopamine electrochemical sensor based on a platinum–silver graphene nanocomposite modified electrode. *Rsc Advances*, 10(29), 17336-17344.
- Araby, S., Meng, Q., Zhang, L., Kang, H., Majewski, P., Tang, Y., & Ma, J. (2014). Electrically and thermally conductive elastomer/graphene nanocomposites by solution mixing. *Polymer*, 55(1), 201-210.
- Arumugasamy, S. K., Govindaraju, S., & Yun, K. (2020). Electrochemical sensor for detecting dopamine using graphene quantum dots incorporated with multiwall carbon nanotubes. *Applied Surface Science*, 508, 145294.
- Ashraf, A., Jani, N., Farmer, F., & Lynch-Branzoi, J. K. (2020). Non-destructive investigation of dispersion, bonding, and thermal properties of emerging polymer nanocomposites using close-up lens assisted infrared thermography. *MRS Advances*, 5(14-15), 735-742.

- Atta, N. F., Galal, A., & El-Said, D. M. (2019). Novel design of a layered electrochemical dopamine sensor in real samples based on gold nanoparticles/ β -cyclodextrin/nafion-modified gold electrode. *ACS omega*, 4(19), 17947-17955.
- Aydın, E. B., Aydın, M., & Sezgintürk, M. K. (2017). A highly sensitive immunosensor based on ITO thin films covered by a new semi-conductive conjugated polymer for the determination of TNF α in human saliva and serum samples. *Biosensors and Bioelectronics*, 97, 169-176.
- Baker, E. A., & Leaper, D. J. (2000). Proteinases, their inhibitors, and cytokine profiles in acute wound fluid. *Wound repair and regeneration*, 8(5), 392-398.
- Bala, K., Sharma, D., & Gupta, N. (2019). Carbon-Nanotube-Based Materials for Electrochemical Sensing of the Neurotransmitter Dopamine. *ChemElectroChem*, 6(2), 274-288.
- Balkwill, F. (2006). TNF- α in promotion and progression of cancer. *Cancer and Metastasis Reviews*, 25(3), 409-416.
- Barrientos, S., Stojadinovic, O., Golinko, M. S., Brem, H., & Tomic-Canic, M. (2008). Growth factors and cytokines in wound healing. *Wound repair and regeneration*, 16(5), 585-601.
- Barton, B. E. (2001). IL-6-like cytokines and cancer cachexia. *Immunologic research*, 23(1), 41-58.
- Bogomolova, A., Komarova, E., Reber, K., Gerasimov, T., Yavuz, O., Bhatt, S., & Aldissi, M. (2009). Challenges of electrochemical impedance spectroscopy in protein biosensing. *Analytical Chemistry*, 81(10), 3944-3949.
- Briscoe, J., & Dunn, S. (2015). Piezoelectric nanogenerators—a review of nanostructured piezoelectric energy harvesters. *Nano Energy*, 14, 15-29.
- Broadhurst, M., & Davis, G. (1984). Physical basis for piezoelectricity in PVDF. *Ferroelectrics*, 60(1), 3-13.
- Caporali, R., Pallavicini, F. B., Filippini, M., Gorla, R., Marchesoni, A., Favalli, E. G., Sarzi-Puttini, P., Atzeni, F., & Montecucco, C. (2009). Treatment of rheumatoid arthritis with anti-TNF-alpha agents: a reappraisal. *Autoimmunity reviews*, 8(3), 274-280.
- Cate, D. M., Adkins, J. A., Mettakoonpitak, J., & Henry, C. S. (2015). Recent developments in paper-based microfluidic devices. *Analytical Chemistry*, 87(1), 19-41.
- Cha, S. M., Nagaraju, G., Sekhar, S. C., & Yu, J. S. (2017). A facile drop-casting approach to nanostructured copper oxide-painted conductive woven textile as binder-free electrode for improved energy storage performance in redox-additive electrolyte. *Journal of Materials Chemistry A*, 5(5), 2224-2234.
- Chang, W.-Y., & Hsu, C.-H. (2013). Electromechanical characteristics of Polyvinylidene Fluoride for flexible electronics. *Transactions of the Canadian Society for Mechanical Engineering*, 37(3), 325-333.
- Cho, K. H., Yu, H., Lee, J. S., & Jang, J. (2020). Facile synthesis of palladium-decorated three-dimensional conducting polymer nanofilm for highly sensitive H₂ gas sensor. *Journal of Materials Science*, 55(12), 5156-5165.
- Choudhary, M., Brink, R., Nandi, D., Siwal, S., & Mallick, K. (2017). Gold nanoparticle within the polymer chain, a multi-functional composite material, for the electrochemical detection of dopamine and the hydrogen atom-mediated reduction of Rhodamine-B, a mechanistic approach. *Journal of Materials Science*, 52(2), 770-781.
- Clemens, S., Rye, D., & Hochman, S. (2006). Restless legs syndrome: revisiting the dopamine hypothesis from the spinal cord perspective. *Neurology*, 67(1), 125-130.

- Cohen, J. D., Bournierias, I., Buffard, V., Paufler, A., Chevalier, X., Bagot, M., & Claudepierre, P. (2007). Psoriasis induced by tumor necrosis factor- α antagonist therapy: a case series. *The Journal of Rheumatology*, 34(2), 380-385.
- Cruceriu, D., Baldasici, O., Balacescu, O., & Berindan-Neagoe, I. (2020). The dual role of tumor necrosis factor- α (TNF- α) in breast cancer: molecular insights and therapeutic approaches. *Cellular Oncology*, 43, 1-18.
- Davis, K. L., Kahn, R. S., Ko, G., & Davidson, M. (1991). Dopamine in schizophrenia: a review and reconceptualization. *The American journal of psychiatry*.
- Du, Y., Dai, L., Yang, F., Zhang, Y., & An, C. (2022). In-situ polymerization confining synthesis of ultrasmall MoTe₂ nanoparticles for electrochemical detection of dopamine. *Inorganic Chemistry Frontiers*.
- Dungchai, W., Chailapakul, O., & Henry, C. S. (2009). Electrochemical detection for paper-based microfluidics. *Analytical Chemistry*, 81(14), 5821-5826.
- Dungchai, W., Chailapakul, O., & Henry, C. S. (2011). A low-cost, simple, and rapid fabrication method for paper-based microfluidics using wax screen-printing. *Analyst*, 136(1), 77-82.
- Fabregat, G., Casanovas, J., Redondo, E., Armelin, E., & Alemán, C. (2014). A rational design for the selective detection of dopamine using conducting polymers. *Physical Chemistry Chemical Physics*, 16(17), 7850-7861.
- Fan, F. R., Tang, W., & Wang, Z. L. (2016). Flexible nanogenerators for energy harvesting and self-powered electronics. *Advanced Materials*, 28(22), 4283-4305.
- Fang, M., Xiong, X., Hao, Y., Zhang, T., Wang, H., Cheng, H.-M., & Zeng, Y. (2019). Preparation of highly conductive graphene-coated glass fibers by sol-gel and dip-coating method. *Journal of Materials Science & Technology*, 35(9), 1989-1995.
- Farivar, F., Yap, P. L., Hassan, K., Tung, T. T., Tran, D. N., Pollard, A. J., & Losic, D. (2021). Unlocking thermogravimetric analysis (TGA) in the fight against “Fake graphene” materials. *Carbon*, 179, 505-513.
- Feldmann, M., & Maini, R. N. (2001). Anti-TNF (alpha) therapy or rheumatoid arthritis: What have we learned? *Annual review of immunology*, 19, 163.
- Figueira, J., Loureiro, J., Vieira, E., Fortunato, E., Martins, R., & Pereira, L. (2022). Flexible, scalable, and efficient thermoelectric touch detector based on PDMS and graphite flakes. *Flexible and Printed Electronics*, 6(4), 045018.
- Gheibi, A., Bagherzadeh, R., Merati, A. A., & Latifi, M. (2014). Electrical power generation from piezoelectric electrospun nanofibers membranes: electrospinning parameters optimization and effect of membranes thickness on output electrical voltage. *Journal of Polymer Research*, 21(11), 1-14.
- Ghosh, D., Rahman, M. A., Ashraf, A., & Islam, N. (2022). Hydrogel and Graphene Embedded Piezoresistive Microcantilever Sensor for Solvent and Gas Flow Detection. International Manufacturing Science and Engineering Conference,
- Grayson, L., Hansbrough, J., Zapata-Sirvent, R., Dore, C., Morgan, J., & Nicolson, M. (1993). Quantitation of cytokine levels in skin graft donor site wound fluid. *Burns*, 19(5), 401-405.
- Grimstad, Ø., Sandanger, Ø., Ryan, L., Otterdal, K., Damaas, J. K., Pukstad, B., & Espevik, T. (2011). Cellular sources and inducers of cytokines present in acute wound fluid. *Wound repair and regeneration*, 19(3), 337-347.

- Gualandi, I., Tonelli, D., Mariani, F., Scavetta, E., Marzocchi, M., & Fraboni, B. (2016). Selective detection of dopamine with an all PEDOT: PSS organic electrochemical transistor. *Scientific reports*, 6(1), 1-10.
- Guo, H.-F., Li, Z.-S., Dong, S.-W., Chen, W.-J., Deng, L., Wang, Y.-F., & Ying, D.-J. (2012). Piezoelectric PU/PVDF electrospun scaffolds for wound healing applications. *Colloids and Surfaces B: Biointerfaces*, 96, 29-36.
- Hakimi, M., Salehi, A., & Boroumand, F. A. (2016). Fabrication and characterization of an ammonia gas sensor based on PEDOT-PSS with N-doped graphene quantum dots dopant. *IEEE Sensors Journal*, 16(16), 6149-6154.
- Hayashi, Y., Matsuda, R., Ito, K., Nishimura, W., Imai, K., & Maeda, M. (2005). Detection limit estimated from slope of calibration curve: an application to competitive ELISA. *Analytical sciences*, 21(2), 167-169.
- Huang, J., Chen, H., Niu, W., Fam, D. W., Palaniappan, A., Larisika, M., Faulkner, S. H., Nowak, C., Nimmo, M. A., & Liedberg, B. (2015). Highly manufacturable graphene oxide biosensor for sensitive Interleukin-6 detection. *Rsc Advances*, 5(49), 39245-39251.
- Jang, H., Park, Y. J., Chen, X., Das, T., Kim, M.-S., & Ahn, J.-H. (2016). Graphene-Based Flexible and Stretchable Electronics. 28(22), 4184-4202.
<https://doi.org/doi:10.1002/adma.201504245>
- Jengelly, D. H., & Zimmers, T. A. (2022). The Role of Interleukin-6/GP130 Cytokines in Cancer Cachexia. In *The Systemic Effects of Advanced Cancer: A Textbook on Cancer-Associated Cachexia* (pp. 97-117). Springer.
- Jin, C., Hao, N., Xu, Z., Trase, I., Nie, Y., Dong, L., Closson, A., Chen, Z., & Zhang, J. X. (2020). Flexible piezoelectric nanogenerators using metal-doped ZnO-PVDF films. *Sensors and Actuators A: Physical*, 305, 111912.
- Karuwan, C., Sriprachuabwong, C., Wisitsoraat, A., Phokharatkul, D., Sritongkham, P., & Tuantranont, A. (2012). Inkjet-printed graphene-poly (3, 4-ethylenedioxythiophene): poly (styrene-sulfonate) modified on screen printed carbon electrode for electrochemical sensing of salbutamol. *Sensors and Actuators B: Chemical*, 161(1), 549-555.
- Khalifa, M., & Anandhan, S. (2019). PVDF nanofibers with embedded polyaniline-graphitic carbon nitride nanosheet composites for piezoelectric energy conversion. *ACS Applied Nano Materials*, 2(11), 7328-7339.
- Khalifa, M., Mahendran, A., & Anandhan, S. (2019). Durable, efficient, and flexible piezoelectric nanogenerator from electrospun PANi/HNT/PVDF blend nanocomposite. *Polymer Composites*, 40(4), 1663-1675.
- Kinlen, P., Liu, J., Ding, Y., Graham, C., & Remsen, E. (1998). Emulsion polymerization process for organically soluble and electrically conducting polyaniline. *Macromolecules*, 31(6), 1735-1744.
- Knüpfer, H., & Preiß, R. (2007). Significance of interleukin-6 (IL-6) in breast cancer. *Breast cancer research and treatment*, 102(2), 129-135.
- Kongsuphol, P., Ng, H. H., Pursey, J. P., Arya, S. K., Wong, C. C., Stulz, E., & Park, M. K. (2014). EIS-based biosensor for ultra-sensitive detection of TNF- α from non-diluted human serum. *Biosensors and Bioelectronics*, 61, 274-279.
- Kumar, S., Kumar, S., Pandey, C. M., & Malhotra, B. D. (2016). Conducting paper based sensor for cancer biomarker detection. *Journal of Physics: Conference Series*,
- Kumar, V., Alam, M. N., Manikkavel, A., Choi, J., & Lee, D. J. (2021). Investigation of silicone rubber composites reinforced with carbon nanotube, nanographite, their hybrid, and

- applications for flexible devices. *Journal of Vinyl and Additive Technology*, 27(2), 254-263.
- Kurian, A. S., Mohan, V. B., Souri, H., Leng, J., & Bhattacharyya, D. (2020). Multifunctional flexible and stretchable graphite-silicone rubber composites. *Journal of Materials Research and Technology*, 9(6), 15621-15630.
- Lakshmi, D., Bossi, A., Whitcombe, M. J., Chianella, I., Fowler, S. A., Subrahmanyam, S., Piletska, E. V., & Piletsky, S. A. (2009). Electrochemical sensor for catechol and dopamine based on a catalytic molecularly imprinted polymer-conducting polymer hybrid recognition element. *Analytical Chemistry*, 81(9), 3576-3584.
- Lee, I., & Sung, H. J. (1999). Development of an array of pressure sensors with PVDF film. *Experiments in Fluids*, 26(1), 27-35.
- Li, X., Zhang, R., Yu, W., Wang, K., Wei, J., Wu, D., Cao, A., Li, Z., Cheng, Y., Zheng, Q., Ruoff, R. S., & Zhu, H. (2012). Stretchable and highly sensitive graphene-on-polymer strain sensors [Article]. *Scientific Reports*, 2, 870. <https://doi.org/10.1038/srep00870>
<https://www.nature.com/articles/srep00870#supplementary-information>
- Liang, T., Pal, R. K., Zou, X., Root, A., Mazzeo, A. D., Hussain, M., & El-Atab, N. (2019). Flexible and Stretchable Paper-based Structures for Electronic Applications. In *Handbook of Flexible and Stretchable Electronics* (pp. 337-375). CRC Press Boca Raton, FL, USA.
- Liang, T., Zou, X., Pal, R. K., Xie, J., Assasie-Gyimah, M. K., Liu, J., Guo, W., Chen, C., Tenorio, M., & Sullivan, D. (2020). Tunable electrical properties of embossed, cellulose-based paper for skin-like sensing. *ACS Applied Materials & Interfaces*, 12(46), 51960-51968.
- Lin, K.-C., Tsai, T.-H., & Chen, S.-M. (2010). Performing enzyme-free H₂O₂ biosensor and simultaneous determination for AA, DA, and UA by MWCNT–PEDOT film. *Biosensors and Bioelectronics*, 26(2), 608-614.
- Liu, K., Yang, C., Song, L., Wang, Y., Wei, Q., Deng, Q., & Hu, N. (2022). Highly stretchable, superhydrophobic and wearable strain sensors based on the laser-irradiated PDMS/CNT composite. *Composites Science and Technology*, 218, 109148.
- Liu, Y., Zhou, Q., & Revzin, A. (2013). An aptasensor for electrochemical detection of tumor necrosis factor in human blood. *Analyst*, 138(15), 4321-4326.
- Longo, A., Baraket, A., Vatteroni, M., Zine, N., Baussells, J., Di Francesco, F., Karanasiou, G. S., Fotiadis, D. I., Mencias, A., & Errachid, A. (2016). Highly sensitive electrochemical BioMEMS for TNF- α detection in humansaliva: heart failure. *Procedia Engineering*, 168, 97-100.
- Loo, S. W., & Pui, T.-S. (2020). Cytokine and cancer biomarkers detection: the dawn of electrochemical paper-based biosensor. *Sensors*, 20(7), 1854.
- López-Honorato, E., Meadows, P., Shatwell, R., & Xiao, P. (2010). Characterization of the anisotropy of pyrolytic carbon by Raman spectroscopy. *Carbon*, 48(3), 881-890.
- Lotharius, J., & Brundin, P. (2002). Pathogenesis of Parkinson's disease: dopamine, vesicles and α -synuclein. *Nature Reviews Neuroscience*, 3(12), 932-942.
- Lou, Y., He, T., Jiang, F., Shi, J.-J., & Zhu, J.-J. (2014). A competitive electrochemical immunosensor for the detection of human interleukin-6 based on the electrically heated carbon electrode and silver nanoparticles functionalized labels. *Talanta*, 122, 135-139.
- Lu, L., Ding, W., Liu, J., & Yang, B. (2020). Flexible PVDF based piezoelectric nanogenerators. *Nano Energy*, 105251.

- Lu, Y., Biswas, M. C., Guo, Z., Jeon, J.-W., & Wujcik, E. K. (2019). Recent developments in bio-monitoring via advanced polymer nanocomposite-based wearable strain sensors. *Biosensors and Bioelectronics*, 123, 167-177.
<https://doi.org/https://doi.org/10.1016/j.bios.2018.08.037>
- Luong, J. H., Narayan, T., Solanki, S., & Malhotra, B. D. (2020). Recent advances of conducting polymers and their composites for electrochemical biosensing applications. *Journal of Functional Biomaterials*, 11(4), 71.
- Lynch-Branzoi, J. K., Ashraf, A., Tewatia, A., Taghon, M., Wooding, J., Hendrix, J., Kear, B. H., & Nosker, T. J. (2020). Shear exfoliation of graphite into graphene nanoflakes directly within polyetheretherketone and a spectroscopic study of this high modulus, lightweight nanocomposite. *Composites Part B: Engineering*, 188, 107842.
- Maccioni, R. B., Rojo, L. E., Fernandez, J. A., & Kuljis, R. O. (2009). The role of neuroimmunomodulation in Alzheimer's disease. *Annals of the New York Academy of Sciences*, 1153(1), 240-246.
- Mahalakshmi, S., & Sridevi, V. (2021). In situ electrodeposited gold nanoparticles on polyaniline-modified electrode surface for the detection of dopamine in presence of ascorbic acid and uric acid. *Electrocatalysis*, 12(4), 415-435.
- Mahapatra, B., Patel, K. K., & Patel, P. K. (2021). A review on recent advancement in materials for piezoelectric/triboelectric nanogenerators. *Materials Today: Proceedings*, 46, 5523-5529.
- Malmonge, L. F., Langiano, S. d. C., Cordeiro, J. M. M., Mattoso, L. H. C., & Malmonge, J. A. (2010). Thermal and mechanical properties of PVDF/PANI blends. *Materials Research*, 13(4), 465-470.
- Mantione, D., Del Agua, I., Sanchez-Sanchez, A., & Mecerreyes, D. (2017). Poly (3, 4-ethylenedioxythiophene)(PEDOT) derivatives: Innovative conductive polymers for bioelectronics. *Polymers*, 9(8), 354.
- Mazloum-Ardakani, M., & Hosseinzadeh, L. (2015). Highly-sensitive label-free immunosensor for tumor necrosis factor α based on Ag@ Pt core-shell nanoparticles supported on MWCNTs as an efficient electrocatalyst nanocomposite. *Rsc Advances*, 5(87), 70781-70786.
- Mazzeo, A. D., Liang, T., Zou, X., Xie, J., Ashraf, A., Salvi, D., Berthiaume, F., & Pal, R. K. (2021). Paper as a substrate and smart material for electronics, packaging, and robotics. 2021 IEEE International Conference on Flexible and Printable Sensors and Systems (FLEPS),
- Merlini, C., Barra, G. M. d. O., Ramôa, S. D. A. d. S., Contri, G., Almeida, R. d. S., d'Ávila, M. A., & Soares, B. G. (2015). Electrically conductive polyaniline-coated electrospun poly (vinylidene fluoride) mats. *Frontiers in Materials*, 2, 14.
- Morais, R. M., dos Santos Klem, M., Nogueira, G. L., Gomes, T. C., & Alves, N. (2018). Low cost humidity sensor based on PANI/PEDOT: PSS printed on paper. *IEEE Sensors Journal*, 18(7), 2647-2651.
- Moran, C. G., Ballesteros, R. G., & Gomez, E. S. (2004). Polivinyldene difluoride (PVDF) pressure sensor for biomedical applications. (ICEEE). 1st International Conference on Electrical and Electronics Engineering, 2004.,
- Mullaveettil, F. N., Dauksevicius, R., & Wakjira, Y. (2021). Strength and elastic properties of 3D printed PVDF-based parts for lightweight biomedical applications. *Journal of the Mechanical Behavior of Biomedical Materials*, 120, 104603.

- Munteanu, I. G., & Apetrei, C. (2022). A review on electrochemical sensors and biosensors used in assessing antioxidant activity. *Antioxidants*, 11(3), 584.
- Murayama, N., Nakamura, K., Obara, H., & Segawa, M. (1976). The strong piezoelectricity in polyvinylidene fluoride (PVDF). *Ultrasonics*, 14(1), 15-24.
- Omi, F. R., Choudhury, M. R., Anwar, N., Bakr, A. R., & Rahaman, M. S. (2017). Highly conductive ultrafiltration membrane via vacuum filtration assisted layer-by-layer deposition of functionalized carbon nanotubes. *Industrial & Engineering Chemistry Research*, 56(30), 8474-8484.
- Pan, X., Wang, Z., Cao, Z., Zhang, S., He, Y., Zhang, Y., Chen, K., Hu, Y., & Gu, H. (2016). A self-powered vibration sensor based on electrospun poly (vinylidene fluoride) nanofibres with enhanced piezoelectric response. *Smart Materials and Structures*, 25(10), 105010.
- Pandikumar, A., How, G. T. S., See, T. P., Omar, F. S., Jayabal, S., Kamali, K. Z., Yusoff, N., Jamil, A., Ramaraj, R., & John, S. A. (2014). Graphene and its nanocomposite material based electrochemical sensor platform for dopamine. *Rsc Advances*, 4(108), 63296-63323.
- Papageorgiou, D. G., Kinloch, I. A., & Young, R. J. (2015). Graphene/elastomer nanocomposites. *Carbon*, 95, 460-484.
<https://doi.org/https://doi.org/10.1016/j.carbon.2015.08.055>
- Pascual, M., Nieto, A., Mataran, L., Balsa, A., Pascual-Salcedo, D., & Martin, J. (2000). IL-6 promoter polymorphisms in rheumatoid arthritis. *Genes & Immunity*, 1(5), 338-340.
- Paton, K. R., Varrla, E., Backes, C., Smith, R. J., Khan, U., O'Neill, A., Boland, C., Lotya, M., Istrate, O. M., & King, P. (2014). Scalable production of large quantities of defect-free few-layer graphene by shear exfoliation in liquids. *Nature materials*, 13(6), 624-630.
- Peng, J., Feng, L. N., Ren, Z. J., Jiang, L. P., & Zhu, J. J. (2011). Synthesis of Silver Nanoparticle-Hollow Titanium Phosphate Sphere Hybrid as a Label for Ultrasensitive Electrochemical Detection of Human Interleukin-6. *Small*, 7(20), 2921-2928.
- Popa, C., Netea, M. G., Van Riel, P. L., Van Der Meer, J. W., & Stalenhoef, A. F. (2007). The role of TNF- α in chronic inflammatory conditions, intermediary metabolism, and cardiovascular risk. *Journal of lipid research*, 48(4), 751-762.
- Puértolas, J., García-García, J., Pascual, F. J., González-Domínguez, J. M., Martínez, M., & Ansón-Casaos, A. (2017). Dielectric behavior and electrical conductivity of PVDF filled with functionalized single-walled carbon nanotubes. *Composites Science and Technology*, 152, 263-274.
- Pui, T. S., Kongsuphol, P., Arya, S. K., & Bansal, T. (2013). Detection of tumor necrosis factor (TNF- α) in cell culture medium with label free electrochemical impedance spectroscopy. *Sensors and Actuators B: Chemical*, 181, 494-500.
- Pullano, S. A., Mahbub, I., Islam, S. K., & Fiorillo, A. S. (2017). PVDF sensor stimulated by infrared radiation for temperature monitoring in microfluidic devices. *Sensors*, 17(4), 850.
- Rahimzadeh, Z., Naghib, S. M., Zare, Y., & Rhee, K. Y. (2020). An overview on the synthesis and recent applications of conducting poly (3, 4-ethylenedioxythiophene)(PEDOT) in industry and biomedicine. *Journal of Materials Science*, 55(18), 7575-7611.
- Rahman, M. A., Becerril, J., Ghosh, D., Islam, N., & Ashraf, A. (2022). Non-Destructive Infrared Thermographic Curing Analysis of Polymer Composites. ASME International Mechanical Engineering Congress and Exposition,

- Rahman, M. A., Rahman, M. M., & Ashraf, A. (2023). Automatic dispersion, defect, curing, and thermal characteristics determination of polymer composites using micro-scale infrared thermography and machine learning algorithm. *Scientific Reports*, 13(1), 2787.
- Rahman, M. A., Rubaiya, F., Islam, N., Lozano, K., & Ashraf, A. (2022). Graphene-Coated PVDF/PAni Fiber Mats and Their Applications in Sensing and Nanogeneration. *ACS applied materials & interfaces*, 14(33), 38162-38171.
- Rather, M. A., Bhat, S. A., Pandit, S. A., Rather, G. M., Khan, K. Z., & Bhat, M. A. (2017). Imidazolium based surface active ionic liquids as novel micellar media for simultaneous and sensitive electrochemical detection of dopamine and ascorbic acid. *Electroanalysis*, 29(7), 1772-1782.
- Ruecha, N., Shin, K., Chailapakul, O., & Rodthongkum, N. (2019). Label-free paper-based electrochemical impedance immunosensor for human interferon gamma detection. *Sensors and Actuators B: Chemical*, 279, 298-304.
- Russell, C., Ward, A. C., Vezza, V., Hoskisson, P., Alcorn, D., Steenson, D. P., & Corrigan, D. K. (2019). Development of a needle shaped microelectrode for electrochemical detection of the sepsis biomarker interleukin-6 (IL-6) in real time. *Biosensors and Bioelectronics*, 126, 806-814.
- Russell, S. M., Alba-Patiño, A., Barón, E., Borges, M., Gonzalez-Freire, M., & De La Rica, R. (2020). Biosensors for managing the COVID-19 cytokine storm: challenges ahead. *ACS sensors*, 5(6), 1506-1513.
- Ryu, G. H., Lee, J., Kang, D., Jo, H. J., Shin, H. S., & Lee, Z. (2017). Effects of dry oxidation treatments on monolayer graphene. *2D Materials*, 4(2), 024011.
- Sadasivuni, K. K., Ponnamm, D., Thomas, S., & Grohens, Y. (2014). Evolution from graphite to graphene elastomer composites. *Progress in Polymer Science*, 39(4), 749-780. <https://doi.org/10.1016/j.progpolymsci.2013.08.003>
- Sarkar, K., Gomez, C., Zambrano, S., Ramirez, M., de Hoyos, E., Vasquez, H., & Lozano, K. (2010). Electrospinning to forcespinning™. *Materials today*, 13(11), 12-14.
- Sengupta, D., Kottapalli, A. G. P., Chen, S. H., Miao, J. M., Kwok, C. Y., Triantafyllou, M. S., Warkiani, M. E., & Asadnia, M. (2017). Characterization of single polyvinylidene fluoride (PVDF) nanofiber for flow sensing applications. *AIP Advances*, 7(10), 105205.
- Shao, D., Sheng, G., Chen, C., Wang, X., & Nagatsu, M. (2010). Removal of polychlorinated biphenyls from aqueous solutions using β -cyclodextrin grafted multiwalled carbon nanotubes. *Chemosphere*, 79(7), 679-685.
- Shen, X., Ju, F., Li, G., & Ma, L. (2020). Smartphone-based electrochemical potentiostat detection system using PEDOT: PSS/chitosan/graphene modified screen-printed electrodes for dopamine detection. *Sensors*, 20(10), 2781.
- Shirinov, A. V., & Schomburg, W. K. (2008). Pressure sensor from a PVDF film. *Sensors and Actuators A: Physical*, 142(1), 48-55.
- Singh, V., Mohan, S., Singh, G., Pandey, P., & Prakash, R. (2008). Synthesis and characterization of polyaniline-carboxylated PVC composites: application in development of ammonia sensor. *Sensors and Actuators B: Chemical*, 132(1), 99-106.
- Subramania, A., & Devi, S. L. (2008). Polyaniline nanofibers by surfactant-assisted dilute polymerization for supercapacitor applications. *Polymers for Advanced Technologies*, 19(7), 725-727.

- Tang, Z. H., Zhang, L. Q., Feng, W. J., Guo, B. C., Liu, F., & Jia, D. M. (2014). Rational Design of Graphene Surface Chemistry for High-Performance Rubber/Graphene Composites. *Macromolecules*, 47(24), 8663-8673. <https://doi.org/10.1021/maS02201e>
- Thomsen, C., & Reich, S. (2000). Double resonant Raman scattering in graphite. *Physical review letters*, 85(24), 5214.
- Ueberschlag, P. (2001). PVDF piezoelectric polymer. *Sensor review*.
- Vinogradov, A., & Holloway, F. (1999). Electro-mechanical properties of the piezoelectric polymer PVDF. *Ferroelectrics*, 226(1), 169-181.
- Voiry, D., Yang, J., Kupferberg, J., Fullon, R., Lee, C., Jeong, H. Y., Shin, H. S., & Chhowalla, M. (2016). High-quality graphene via microwave reduction of solution-exfoliated graphene oxide. *Science*, 353(6306), 1413-1416.
- Wang, G., Huang, H., Zhang, G., Zhang, X., Fang, B., & Wang, L. (2011). Dual amplification strategy for the fabrication of highly sensitive interleukin-6 amperometric immunosensor based on poly-dopamine. *Langmuir*, 27(3), 1224-1231.
- Wang, J., Liu, G., Engelhard, M. H., & Lin, Y. (2006). Sensitive immunoassay of a biomarker tumor necrosis factor- α based on poly (guanine)-functionalized silica nanoparticle label. *Analytical Chemistry*, 78(19), 6974-6979.
- Wang, W., Xu, G., Cui, X. T., Sheng, G., & Luo, X. (2014). Enhanced catalytic and dopamine sensing properties of electrochemically reduced conducting polymer nanocomposite doped with pure graphene oxide. *Biosensors and Bioelectronics*, 58, 153-156.
- Wang, Y., Luo, J., Liu, J., Sun, S., Xiong, Y., Ma, Y., Yan, S., Yang, Y., Yin, H., & Cai, X. (2019). Label-free microfluidic paper-based electrochemical aptasensor for ultrasensitive and simultaneous multiplexed detection of cancer biomarkers. *Biosensors and Bioelectronics*, 136, 84-90.
- Wang, Y., Wang, L., Yang, T., Li, X., Zang, X., Zhu, M., Wang, K., Wu, D., & Zhu, H. (2014). Wearable and Highly Sensitive Graphene Strain Sensors for Human Motion Monitoring. 24(29), 4666-4670. <https://doi.org/doi:10.1002/adfm.201400379>
- Wang, Y., Zheng, J., Ren, G., Zhang, P., & Xu, C. (2011). A flexible piezoelectric force sensor based on PVDF fabrics. *Smart Materials and Structures*, 20(4), 045009.
- Weaver, C., Li, H., Luo, X., & Cui, X. (2014). A graphene oxide/conducting polymer nanocomposite for electrochemical dopamine detection: origin of improved sensitivity and specificity. *Journal of Materials Chemistry B*, 2(32), 5209-5219.
- Weng, S., Chen, M., Zhao, C., Liu, A., Lin, L., Liu, Q., Lin, J., & Lin, X. (2013). Label-free electrochemical immunosensor based on K₃ [Fe (CN) ₆] as signal for facile and sensitive determination of tumor necrosis factor- α . *Sensors and Actuators B: Chemical*, 184, 1-7.
- Wu, J., Xiao, H., Sun, H., Zou, L., & Zhu, L.-Q. (2012). Role of dopamine receptors in ADHD: a systematic meta-analysis. *Molecular neurobiology*, 45, 605-620.
- Wu, Y., Hsu, S. L., Honeker, C., Bravet, D. J., & Williams, D. S. (2012). The role of surface charge of nucleation agents on the crystallization behavior of poly (vinylidene fluoride). *The Journal of Physical Chemistry B*, 116(24), 7379-7388.
- Xia, K., Zhu, Z., Zhang, H., & Xu, Z. (2018). A triboelectric nanogenerator as self-powered temperature sensor based on PVDF and PTFE. *Applied Physics A*, 124(8), 1-7.
- Xie, P., Tayyab, M., Ashraf, A., Kumar, S., Mazzeo, A., Sengupta, K., Berthiaume, F., & Javanmard, M. (2021). Real time cytokine quantification in wound fluid samples using

- nanowell impedance sensing. 2021 21st International Conference on Solid-State Sensors, Actuators and Microsystems (Transducers),
- Xu, G., Jarjes, Z. A., Desprez, V., Kilmartin, P. A., & Travas-Sejdic, J. (2018). Sensitive, selective, disposable electrochemical dopamine sensor based on PEDOT-modified laser scribed graphene. *Biosensors and Bioelectronics*, 107, 184-191.
- Xue, C., Han, Q., Wang, Y., Wu, J., Wen, T., Wang, R., Hong, J., Zhou, X., & Jiang, H. (2013). Amperometric detection of dopamine in human serum by electrochemical sensor based on gold nanoparticles doped molecularly imprinted polymers. *Biosensors and Bioelectronics*, 49, 199-203.
- Yamada, T., Hayamizu, Y., Yamamoto, Y., Yomogida, Y., Izadi-Najafabadi, A., Futaba, D. N., & Hata, K. (2011). A stretchable carbon nanotube strain sensor for human-motion detection [Article]. *Nature Nanotechnology*, 6, 296.
<https://doi.org/10.1038/nnano.2011.36>
<https://www.nature.com/articles/nnano.2011.36#supplementary-information>
- Yang, J., Zhang, Y., Li, Y., Wang, Z., Wang, W., An, Q., & Tong, W. (2021). Piezoelectric Nanogenerators Based on Graphene Oxide/PVDF Electrospun Nanofiber with Enhanced Performances by In-Situ Reduction. *Materials Today Communications*, 26, 101629.
- Yang, L., Liu, S., Zhang, Q., & Li, F. (2012). Simultaneous electrochemical determination of dopamine and ascorbic acid using AuNPs@ polyaniline core-shell nanocomposites modified electrode. *Talanta*, 89, 136-141.
- Yang, Y., Li, M., & Zhu, Z. (2019). A novel electrochemical sensor based on carbon nanotubes array for selective detection of dopamine or uric acid. *Talanta*, 201, 295-300.
- Yin, Z., Liu, Y., Jiang, L.-P., & Zhu, J.-J. (2011). Electrochemical immunosensor of tumor necrosis factor α based on alkaline phosphatase functionalized nanospheres. *Biosensors and Bioelectronics*, 26(5), 1890-1894.
- Zeng, W., Tao, X.-M., Chen, S., Shang, S., Chan, H. L. W., & Choy, S. H. (2013). Highly durable all-fiber nanogenerator for mechanical energy harvesting. *Energy & Environmental Science*, 6(9), 2631-2638.
- Zeyrek Ongun, M., Oguzlar, S., Doluel, E. C., Kartal, U., & Yurddaskal, M. (2020). Enhancement of piezoelectric energy-harvesting capacity of electrospun β -PVDF nanogenerators by adding GO and rGO. *Journal of Materials Science: Materials in Electronics*, 31(3), 1960-1968.
- Zhang, Y., Jiang, S., Yu, Y., Zeng, Y., Zhang, G., Zhang, Q., & He, J. (2012). Crystallization behavior and phase-transformation mechanism with the use of graphite nanosheets in poly (vinylidene fluoride) nanocomposites. *Journal of Applied Polymer Science*, 125(S1), E314-E319.
- Zhu, Z., Qu, L., Guo, Y., Zeng, Y., Sun, W., & Huang, X. (2010). Electrochemical detection of dopamine on a Ni/Al layered double hydroxide modified carbon ionic liquid electrode. *Sensors and Actuators B: Chemical*, 151(1), 146-152.
- Zou, X., Chen, C., Liang, T., Xie, J., Gillette-Henao, E. N., Oh, J., Tumalle, J., & Mazzeo, A. D. (2018). Paper-Based Resistive Networks for Scalable Skin-Like Sensing. *Advanced Electronic Materials*, 4(8), 1800131.

BIOGRAPHICAL SKETCH

Md Ashiqur Rahman was born in a small village in Satkhira, Bangladesh. He completed his Bachelor of Science in Mechanical Engineering in 2019 from Bangladesh University of Engineering and Technology (BUET), Dhaka, Bangladesh. Later, he worked for glass manufacturing and power generation industry for almost 2 years.

He obtained his Master of Science in Engineering degree from University of Texas Rio Grande Valley (UTRGV), USA in August 2023. He was awarded the prestigious Presidential Research Fellowship (PRF), and he continued his research under the supervision of Dr. Ali Ashraf. After pursuing his masters, he is going to join as a Graduate Research Assistant at Purdue University, West Lafayette, Indiana for his PhD in Mechanical Engineering. He wants to build his career in academia as a researcher. He can be reached out to be at the following email: ashiqme157@gmail.com.